ARL-TR-10028 ● Nov 2024

Assessment of Materials Data for High-Throughput Interfacial Energy Calculations for Prevalent Carbides

by Heather Murdoch, Benjamin Szajewski, Matthew Guziewski, Efrain Hernandez-Rivera, Daniel Field, and Daniel Magagnosc

NOTICES

Disclaimers

The findings in this report are not to be construed as an official Department of the Army position unless so designated by other authorized documents.

Citation of manufacturer's or trade names does not constitute an official endorsement or approval of the use thereof.

Destroy this report when it is no longer needed. Do not return it to the originator.

ARL-TR-10028 ● Nov 2024

Assessment of Materials Data for High-Throughput Interfacial Energy Calculations for Prevalent Carbides

Heather Murdoch, Benjamin Szajewski, Matthew Guziewski, Efrain Hernandez-Rivera, Daniel Field, and Daniel Magagnosc
DEVCOM Army Research Laboratory

REPORT DOCUMENTATION PAGE

1. REPORT DATE	2. REPORT TYPE	3. DATES COVERED	
		START DATE	END DATE
November 2024	Technical Report	9/30/2023	9/29/2024

4. TITLE AND SUBTITLE
Assessment of Materials Data for High-Throughput Interfacial Energy Calculations for Prevalent Carbides

5a. CONTRACT NUMBER	5b. GRANT NUMBER	5c. PROGRAM ELEMENT NUMBER
5d. PROJECT NUMBER	**5e. TASK NUMBER**	**5f. WORK UNIT NUMBER**

6. AUTHOR(S)
Heather Murdoch, Benjamin Szajewski, Matthew Guziewski, Efrain Hernandez-Rivera, Daniel Field, and Daniel Magagnosc

7. PERFORMING ORGANIZATION NAME(S) AND ADDRESS(ES)	8. PERFORMING ORGANIZATION REPORT NUMBER
DEVCOM Army Research Laboratory ATTN: FCDD-RLA-MF Aberdeen Proving Ground, MD 21005	ARL-TR-10028

9. SPONSORING/MONITORING AGENCY NAME(S) AND ADDRESS(ES)	10. SPONSOR/MONITOR'S ACRONYM(S)	11. SPONSOR/MONITOR'S REPORT NUMBER(S)

12. DISTRIBUTION/AVAILABILITY STATEMENT
DISTRIBUTION STATEMENT A. Approved for public release: distribution unlimited.

13. SUPPLEMENTARY NOTES
ORCIDs: Heather Murdoch, 0000-0001-7710-0577; Daniel Field, 0000-0002-8890-4391; Matthew Guziewski, 0000-0002-5761-720X; Efrain Hernandez-Rivera, 0000-0002-7855-1027; Daniel Magagnosc, 0000-0002-1418-9292

14. ABSTRACT
Interfacial energy plays an essential role in the nucleation and growth of secondary phases and their role in mechanical behavior. However, determining interfacial energy via experimental approaches is challenging, requiring alternative computational approaches. The main model for estimating interfacial energies only considers chemical contributions. This approach ignores the elastic strain energy component of interfacial energy, which impacts mechanical properties (e.g., coherency of strengthening precipitates). A high-throughput dislocation mechanics method is implemented for calculating the elastic contributions to interfacial energy. This approach requires the lattice parameter, elastic properties, and an orientation relationship for the matrix and precipitate phase. The viability of using Thermo-Calc for high-throughput estimation of lattice spacing as a function of composition and temperature for a variety of phases is demonstrated. Furthermore, elastic constants for the most common carbides observed in a dataset of quenched and tempered steels are gathered and assessed. Orientation relationships were found in the literature or, in one instance, determined based on the precipitate crystallography. Once the necessary materials properties are assembled, the elastic interfacial energy is calculated for approximately 40,000 carbides. In contrast with the conventional chemical interfacial energy model, all values were found to be reasonable relative to experimental observations.

15. SUBJECT TERMS
Sciences of Extreme Materials, interfacial energy, carbides, steel, orientation relationship, high-throughput, Calculation of Phase Diagram, CALPHAD

16. SECURITY CLASSIFICATION OF:			17. LIMITATION OF ABSTRACT	18. NUMBER OF PAGES
a. REPORT	b. ABSTRACT	C. THIS PAGE		
UNCLASSIFIED	UNCLASSIFIED	UNCLASSIFIED	UU	77

19a. NAME OF RESPONSIBLE PERSON	19b. PHONE NUMBER *(Include area code)*
Heather Murdoch	(410) 306-0699

STANDARD FORM 298 (REV. 5/2020)
Prescribed by ANSI Std. Z39.18

Contents

List of Figures

List of Tables

1. Introduction

Calculation of Phase Diagram (CALPHAD) predictions are effective tools for high-throughput screening of alloy candidates. CALPHAD also enables "data augmentation" through synthetic microstructures (e.g., the expected phases at a given temperature) and improves the interpretability of ML models by incorporating physical mechanisms (e.g., phase transformations). The coupling between CALPHAD-based input features and improved ML predictive capabilities has also expanded in recent years.[1–3] Despite this progress, a significant gap in this approach is that most precipitation-strengthened materials rely on nonequilibrium phases to provide the strengthening (e.g., M_2C in ultra-high strength steel [UHSS] steels or η' in 7xxx aluminum). Most current CALPHAD approaches are based on equilibrium phases and struggle to capture the complex kinetic mechanisms leading to metastable precipitation states. Consequently, additional physics-based information must be incorporated to correctly predict and classify the possible precipitate phases in an alloy system for both strength predictions and optimizing processing routes during alloy design.

Key factors in most precipitate nucleation and growth models are thermodynamic driving force, diffusion coefficients, nucleation site density (NSD), and interfacial energy. Driving force and diffusion are well covered by existing CALPHAD approaches and databases. Conversely, a reasonable NSD, which relates to specific microstructure features, is necessary only when predicting the size and number fraction evolution of a specific precipitate, and not when screening which precipitate phase will form. Determination of interfacial energy is a current capability gap.

The interfacial energy for a precipitate-matrix interface contains both chemical and mechanical contributions. In the CALPHAD Thermo-Calc software, interfacial energy is predicted using the Becker model,[4] which only calculates the chemical contribution to the interfacial energy, assuming a coherent interface, and that the matrix and precipitate are both isotropic. These are simplifying assumptions that underestimate the interfacial energy, especially when the metallic interfaces in question have been experimentally observed to be semicoherent or incoherent. However, this approach does enable high-throughput calculations, unlike experimental measurements or atomistic simulations. Typical experimental approaches require extremely high-fidelity measurements (transmission electron microscopy [TEM] and high-resolution X-ray diffraction [XRD]) and time-consuming preparation of samples.[5–8] Other computational methods (density functional theory [DFT] and molecular dynamics [MD]) are attractive for studying

a limited number of interfaces, but the tradeoffs between high fidelity, computational demands, unphysical thermal environments, manageable supercell construction, simulation time scales, and requisite interatomic potential development limit their utility for screening thousands of interfaces.[9]

Using a dataset of approximately 2000 tempered martensitic steels,[10] we calculated the interfacial energy using the Becker model in Thermo-Calc at the experimentally performed tempering temperatures for the most common carbides. Before considering whether the predictions from this model qualitatively match observations in steels, it was clear from analyzing the results of the Becker calculation (Figure 1) that some predictions were unphysical, i.e., $\sigma > 1$ J/m^2. This can be somewhat mitigated by running a time–temperature–transformation (TTT) curve[11] for the composition and calculating the interfacial energy at the "nose" (i.e., the most favorable temperature). The TTT curve and subsequent nose calculation yield interface energies are mostly below 1 J/m^2, and all below 2 J/m^2; however, it takes considerably more time to calculate (on the order of 10 times longer).

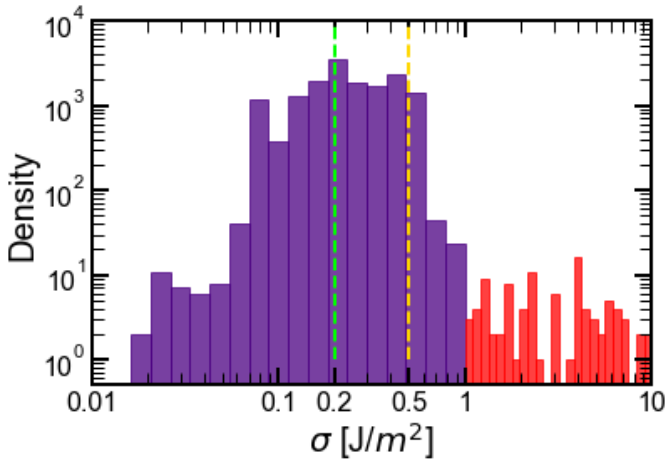

Figure 1. Predicted interfacial energies from Thermo-Calc for ~20,000 carbides in martensitic steels (ref dataset[10]). The interfacial energy cutoff for coherent and semicoherent boundaries are noted with green and yellow dashed lines, respectively. Unphysical predictions are noted in red.

A brief survey of Thermo-Calc's Becker model predictions for some common strengthening carbides (Figure 2) shows some discrepancies with experimental observations (Table 1). Notably the hexagonal close-packed (HCP) M_2C and the face-centered cubic (FCC) MC carbides, which are often experimentally observed to range from coherent to semicoherent (e.g., Mongomery and Olson, and Olson et al.[12,13]) and used as strengthening precipitates in UHSS steels, are predicted by the Becker model to be semicoherent to incoherent. Conversely, $M_{23}C_6$ is often predicted by the Becker model to be coherent, when it is most often observed to be

incoherent.[14] Similarly, the M_6C interfacial energy is predicted to be lower than expected. In a detailed work both experimentally characterizing and performing precipitation modeling, it was further shown that, while the Becker's model prediction for cementite, M_2C, MC, and M_6C produced a realistic balance of phases during competitive precipitation, the model could not correctly predict the $M_{23}C_6$ quantity without increasing its interfacial energy.[15] This shows that only using the chemical contribution from the Becker model may not be a reasonable approximation for use as a physics-based input to ML models.

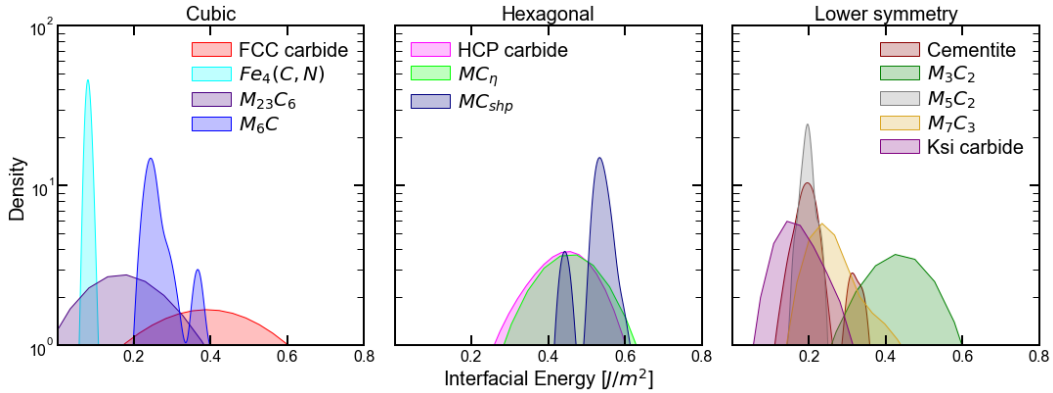

Figure 2. Predicted interfacial energies from Thermo-Calc separated by crystal structure.

Table 1. Example experimental coherencies for common precipitates in body-centered cubic (BCC) matrix for steel along with average prediction from Becker's model. Values are colored by green/yellow/red for coherent/semicoherent/incoherent, respectively.

Precipitate	Experimental coherency[14] (in BCC matrix)	Becker/ chemical model
Fe_3C	semi.	0.21
Fe_4N	semi.	0.07
MC (FCC)	semi.	0.33
M_2C (HCP)	semi.	0.35
M_7C_3	incoh.	0.27
$M_{23}C_6$	incoh.	0.18
M_6C	incoh.	0.28

Even in cases where the Becker model predicts reasonable chemical contributions to interfacial energy, it neglects elastic mismatch entirely, which contributes to the total interfacial energy. This work is motivated by the possibility that considering both the chemical and elastic terms will align the computational predictions better with experimental observations and be more effective for explainability of ML models. Furthermore, introducing an elastic energy term will allow some of the assumptions of the Becker model to be addressed—most notably the assumed isotropic elasticity. This provides the opportunity to account for the diversity of

precipitate configurations, as most strengthening precipitates are not an idealized spherical case (Figure 3). The precipitate configurational anisotropy and orientation relationship (OR) with the matrix are important for the mechanical properties, e.g., determining the modes of dislocation interaction[16]; nanoscale coherent and semicoherent precipitate phases contribute to strengthening. For ML models trained to predict mechanical properties, interactions of dislocations with strengthening precipitates are a key underlying physical mechanism and should be included as a feature in the training process. Further influencing this is the anisotropy of most precipitates, each of which may assume several different ORs with unique interfacial energies.

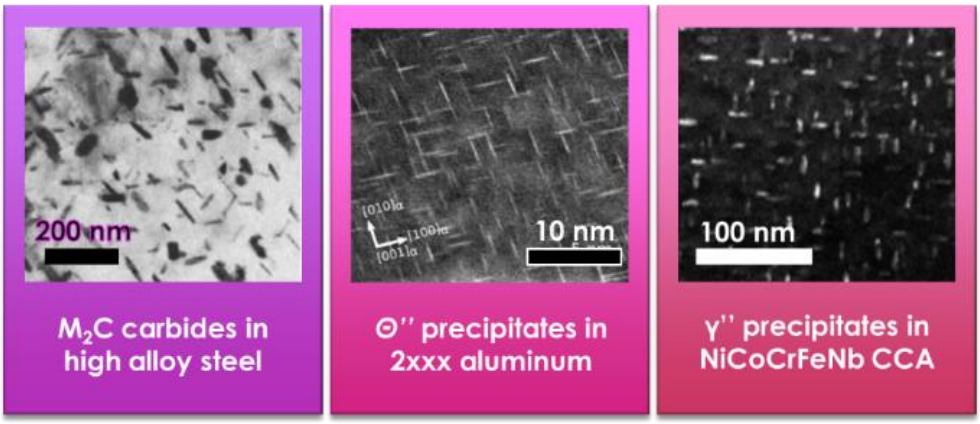

Figure 3. Example strengthening precipitates for the three alloy categories of interest: M_2C in steels,[17] θ'' in 2xxx aluminum,[18] and γ'' in complex concentrated alloys (CCAs).[19]

Therefore, we have developed a mesoscale dislocation-based model to calculate the elastic strain energy contribution to the interfacial energy between a matrix and precipitate of arbitrary crystal structure, which is amenable to high-throughput screening and requires limited materials data as inputs.[20] For each calculation, only the OR, elastic properties, and lattice constants of the matrix and precipitate are required. Having a robust, generalized, high-throughput method to estimate interfacial energy will provide a valuable addition to both precipitation kinetics modelling and ML models.

In this work, the materials parameters necessary for the elastic strain energy calculations for 12 common carbides in steel are compiled and assessed as a case study. First, we demonstrate a methodology for extracting the lattice parameters from Thermo-Calc that can be applied in a high-throughput fashion. Second, the necessary elastic moduli are consolidated. While this contribution is not as amenable to high-throughput calculations, it is demonstrated that this issue may be circumvented by pre-tabulating the parameters. Similarly, we assemble a pre-computed dictionary of ORs. The elastic interfacial energy is then calculated for

approximately 45,000 carbide-matrix combinations as a proof-of-concept of the approach.

2. Methods

2.1 Summary of Elastic Calculation

A detailed description of the dislocation-based approach will be described in another work. Here, a summary is provided to illustrate the workflow and required materials information. A simplified illustration of the precipitate-matrix interface is shown in Figure 4. The precipitate and matrix, with differing unit cell sizes, can be brought into a mutual reference state through the introduction of homogeneous deformations and misfit dislocations. Our approach encompasses dislocation theory[21] and deformation kinematics[22–24] to describe semicoherent interfaces as coherent surfaces separated by localized regions of misfit. Precipitate and matrix kinematic compatibility are achieved through the superposition of homogeneous deformations and periodic arrays of dislocations along the interface (Figure 4). The excess elastic energy created by the deformations and dislocations contribute to the interfacial energy.

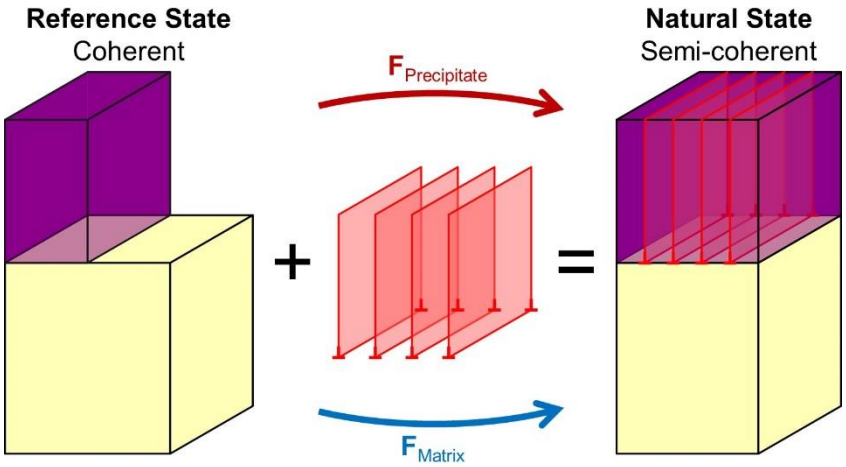

Figure 4. Schematic of simplified precipitate-matrix interface.

Conceptually, the formation of a semicoherent interface may be envisaged as the result of a two-step deformation process. In the first step, a unique homogeneous deformation is applied to the matrix and precipitate bringing them into coherent, perfect crystallographic alignment. This reference state is not stress-free, however. In the second step, two sets of parallel dislocations are added to annul residual far-field stresses. The deformations with accompanying dislocations create a semicoherent interface.

The method used here applies stress-free boundary conditions far from the interface (Equation 1) and the Frank–Bilby equation along the interface (Equation 2). Within the interface plane, the difference in deformations ($\mathbf{F}_A$-$\mathbf{F}_B$) between the matrix and precipitate must be balanced by dislocations to achieve kinematic compatibility. Each of two $\mathbf{b}_i/D_i$ expresses the density of a parallel array of dislocations. The vectors **n,** ξ_i**,** and **p** represent, respectively, a unit normal vector, a vector along the dislocation line direction, and an arbitrary vector in the interface plane. Each $\mathbf{F}_{A,B}$ is a homogeneous deformation between a mutual reference state and individual natural states. Equation 1 expresses the fact that the superposition of dislocation stresses (σ_D) and coherency-induced stresses (σ_C) far from the interface must be zero.

The combination of Equations 1 and 2 describes a linear elastic boundary value problem. The simultaneous solution of these equations yields the dislocation characters ($\xi_i \cdot b_i$) and densities (b_i / D_i) for two parallel arrays of dislocations. Independent of the interface energy, these parameters describe the quality of the fit between the mismatched matrix and precipitate lattices given candidate Burgers vectors. Specifically, each parallelogram formed by the dislocation arrays has a dislocation length of $D_1 + D_2$ and an area of $\frac{D_1 D_2}{|\xi_1 \times \xi_2|}$, where, $|\xi_1 \times \xi_2| = \sin\theta$ represents the sin of the angle (θ) between the two dislocation line directions. Higher dislocation densities correspond to a greater degree of incoherence.

Once Equations 1 and 2 are satisfied, the interface energy (γ) is calculated through averaging the interface energy density ($\triangle u \cdot (\sigma_D + \sigma_C)$) over a unit dislocation cell of area $\frac{D_1 D_2}{|\xi_1 \times \xi_2|}$, as shown in Equation 3. It bears emphasis that the integral extends to each dislocation core. As such, the interface energy, γ, depends on the treatment of the dislocation core energy through σ_D in the vicinity of each dislocation core. As will be demonstrated, both γ and σ_D can exhibit a significant dependence on parameters describing the distribution of the dislocation core.

$$\lim_{z \to \pm\infty} \quad \sigma_D\left(D_{1,2}(\delta), \xi_{1,2}(\delta), b_{1,2}(\delta)\right) + \sigma_C\left(F_{A,B}(\delta)\right) = 0 \tag{1}$$

$$\sum_{i=1}^{2} \frac{n \times \xi_i(\delta) \cdot p}{D_i(\delta)} b_i(\delta) = \left(F_A(\delta) - F_B(\delta)\right)p \tag{2}$$

$$\gamma_{misfit} = \frac{1}{2\iint_{\partial a} dA} \iint_{\partial a} \Delta u \cdot \left(\sigma_D(\delta)|_{z=0} + \sigma_C(\delta)\right) \cdot n dA \tag{3}$$

To apply the outlined approach, three materials parameter sets are required: the (i) lattice parameters, (ii) elastic constants, and a (iii) prescribed OR for a given precipitate-matrix combination. The lattice parameters can be inferred in a high-throughput fashion from the molar volume output from Thermo-Calc. In most cases, application of standard crystallographic information, i.e., the number of

atoms per unit cell and c/a ratio, readily determines the lattice parameters. A major advantage of using the molar volume of the precipitate and matrix from Thermo-Calc is that the lattice constants will then vary with both temperature and composition, improving the specificity of the predictions to a given processing history.

The calculation of the strain energy associated with these misfit dislocations requires elastic properties of both phases, here the shear modulus (μ_i) and Poisson ratio (ν_i). Ideally, these elastic constants will also be functions of temperature and composition. For a limited alloy design space, e.g., the 12 common carbides or commercial precipitation-strengthened aluminums, adequate properties values can be found in literature.

The final requirement is the OR for matrix-precipitate crystal structures. For each matrix-precipitate combination, several candidate ORs are possible. Generating the crystallographic transformations that correspond to each OR is one of the most time-consuming processes as significant initial setup is required. However, this step is amenable to precompiling; once the crystallographic transformations are compiled, subsequent interfacial energy calculations can be run using all possible ORs. The energetically most favorable OR minimizes the interfacial energy while unfeasible ORs produce anomalously high interfacial energies. Thus, by sampling all potential orientations, a true minimum energy and the corresponding OR can be identified, particularly when investigating completely new alloy spaces, such as for precipitation-strengthened CCAs, where the OR is unknown.

2.2 Materials Information

In this work, we focus on carbides in steel as a case study using a dataset of quenched and tempered martensitic steels.[10] To calculate the elastic interfacial energy, the following materials properties are required:

- Shear moduli for the precipitate and the matrix
- Poisson's ratios for the precipitate and the matrix
- Lattice parameters (a, b, c) for the precipitate and the matrix
- OR(s) for each crystal interface

The mechanical properties (shear modulus, μ, and Poisson's ratio, ν) are calculated from the full elastic constants where possible, as detailed in Appendix A. The Hill average[25] is used for the shear modulus. Where possible, we detail the change in mechanical properties with composition and temperature. For example, substituting Cr on the Fe lattice sites in Fe_3C increases the shear modulus even if it does not

significantly affect the lattice parameter.[26,27] We expect the lattice parameters to vary considerably with respect to composition, and to a lesser extent, temperature. That is, changes in lattice parameter with respect to temperature are often driven by compositional variation, as seen in Figure 5. On the left of Figure 5, a straightforward trend can be seen with increasing temperature, where Mn content in the $M_{23}C_6$ phase decreases while the lattice parameter increases. In another alloy, the composition changes considerably with temperature, with a switch from Mn substituting on the Fe sites to Cr and Mo and a corresponding significant jump in the lattice parameter (note the break in the y-axis in Figure 5).

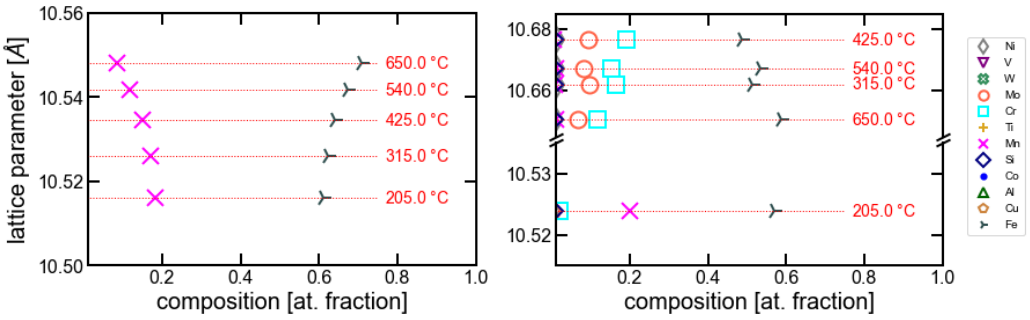

Figure 5. Composition and lattice parameter of $M_{23}C_6$ carbides predicted from Thermo-Calc for two steels (left: American Iron and Steel Institute [AISI] 1144, right: AISI 4340) showing the variability in lattice parameter with temperature is linked to compositional variability.

The shear modulus can also be expected to vary with temperature; however, observed changes with temperature are generally smaller than variations between measurements. For example, in a review of experimental measurements and first-principles calculations of cementite,[28] the shear modulus of Fe_3C only varied from around 71 GPa at room temperature (25 °C) to approximately 67 GPa at 575 °C, for a variation of only approximately 5% over a large temperature range. However, the overall variation in modulus measurements made by different groups was approximately 15% (75 ±11 GPa). Similarly, in tungsten carbide, the shear modulus only decreases by about 4% over the same temperature range.[29] On the other hand, for the α-Fe matrix, the shear modulus decreased 22% (from 81 GPa to 63 GPa) over that same temperature range.[30] Therefore, we will consider the impact of temperature on the shear modulus of the matrix, but not the precipitates.

2.3 Precipitates

2.3.1 Selection of Phases

There is a vast range of possible precipitate phases in steels; to both limit the dimensionality of the materials property space to something tractable (Thermo-Calc 2023b can only support 12 concurrent phases in kinetic simulations), we employ a down-selection procedure.

A dataset of 113 AISI steels (including low alloy, stainless, and tool steels for a large composition range) under various tempering conditions was extracted from the Ansys GRANTA database. The possible phases for each alloy composition and temper temperature combination are determined using Thermo-Calc (TCFE10 database). Across the alloy and temper combinations, 79 possible precipitate phases were identified (including both stable and metastable phases). Next, the possible phases in a system are explored using the Thermo-Calc precipitation module to see if they are kinetically expected to form under the tempering condition for that alloy. The precipitates are then categorized as either likely or unlikely to form, and their population density represented by filled contours or line diagrams, respectively, in Figure 6. If the phase has a high nucleation barrier (or other obstacle to precipitation), the kinetic simulation does not move forward past the initial time step and the precipitate is considered unlikely to form. The phase labels on the plot are the precipitate nomenclature in Thermo-Calc, which generally is of a form containing stoichiometry and a structure factor. It is clear from Figure 6 that only a subset of the possible 79 phases is generally kinetically favorable (11 phases are not depicted in Figure 6 as they did not have enough points to form a density plot, e.g., <5). There are a few interesting trends as to whether certain phases only form in high alloy steels (e.g., CHI_A2) or low temperatures (e.g., HIGH_SIGMA or Z_PHASE).

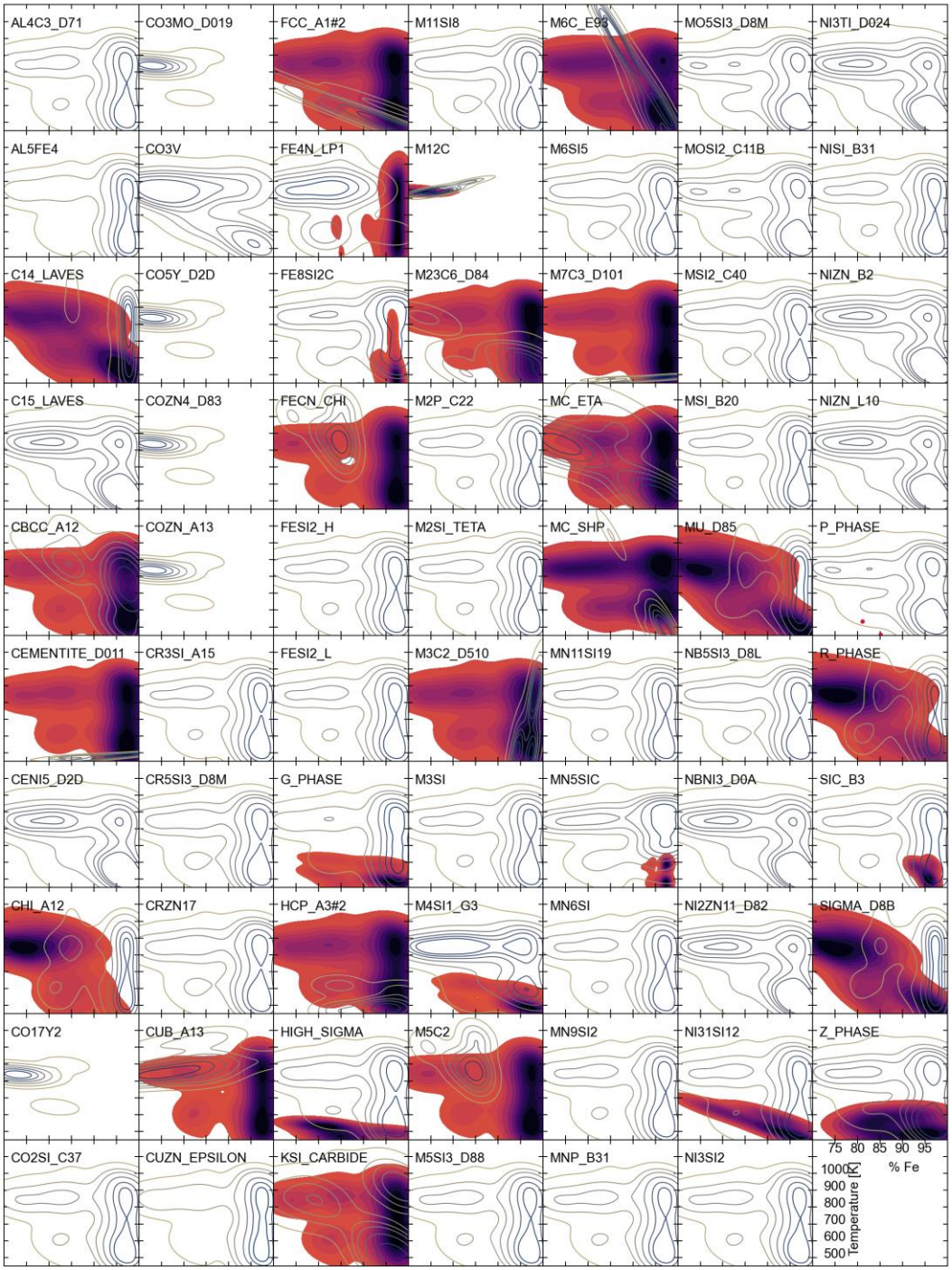

Figure 6. Density plots of possible phases as a function of Fe content in the alloy (wt%) and tempering temperature (K). Colored region indicates kinetically favorable precipitate phases while contour lines indicate phase is possible but not expected to precipitate under the given tempering condition.

Focusing on the phases that have at least some regions of likely formation, we first eliminate those that have instances less than 10% of the total: HIGH_SIGMA, Ni31Si12, P_PHASE, SiC_B3, Z_PHASE, G_PHASE, and M4SI1_G3. Most of

these phases also have a very limited region of possible formation. Other phases with limited regions that still show up more than 10% of the time are FE8SI2C and MN5SIC; despite the potentially favorable conditions for precipitation as determined by the Thermo-Calc databases, carbides in steel that are enriched in silicon are not generally experimentally observed due to uphill diffusion of carbon to avoid silicon.[31] Therefore, we will not consider these phases.

CHI_A12 (χ) is clearly focused on high-alloy and high-temperature regions, so is not relevant across the full alloy space. The C14_LAVES, MU_D85, R_PHASE, and SIGMA_D88 phases have similar patterns and are primarily found in limited temperature and alloy regimes; experimentally, these phases are only expected to be strengthening in high-alloy steels, such as the σ (laves) phase in stainless steels (e.g., Cr >12%). In general, noncarbide phases are generally observed only in high-alloy specialty steels and so we choose to focus on the carbide phases in this work.

Considering the carbides that we have not previously eliminated, the thermodynamic database used in this work is TCFE10; as of 2024, the current release is up to version TCFE13. In the newer databases, the FeCN_CHI phase has been absorbed into M5C2. To be forward compatible, we will do the same; the main difference between the current FeCN and M5C2 is the nitrogen solubility on the sublattice.

For this screening of potential phases for kinetic feasibility and experimental applicability, the 79 secondary phases were down-selected to 12 carbide phases of interest (Table 2).

2.3.2 Information About Phases

Crystallographic information about the 12 down-selected carbides considered in this work are in Table 2. This information is according to the Thermo-Calc database TCFE10; that is, this is the crystal structure and formula unit used to describe the phase in the database, even if there are some variations in what is experimentally observed. The formula unit describes the allowable elements on each sublattice/site; elements that are not present in the dataset[10] have been removed from the "formula unit" for readability. The phases have been organized by crystal structure since that will determine the ORs between precipitate and matrix.

Table 2. Phases considered in this work and their crystallographic information, according to Thermo-Calc database TCFE10.

Phase	Thermo-Calc label	Pearson	Space group (SG)	SG no.	Formula unit
Matrix					
α (ferrite)	BCC_A2	cI2	$Im\bar{3}m$	229	. . .
Orthorhombic precipitates					
Fe_3C (cementite)	CEMENTITE_D011	oP16	Pnma	62	$(Al, Co, Cr, Fe, Mn, Mo, Ni,Si, V, W)_3(B, C, N)_1$
M_3C_2	M3C2_D510	oP20	Pnma	62	$(Co, Cr, Mo, V, W)_3C_2$
M_7C_3	M7C3_D101	oP40	Pnma	62	$(Al, Co, Cr, Fe, Mn, Mo, Ni,Si, V, W)_7(B, C)_3$
Cubic precipitates					
MC (FCC)	FCC_A1#N*	cF4	$Fm\bar{3}m$	225	$(Al, Co, Cr, Cu, Fe, Mn, Mo, Ni, S, Si, Ti, V, W)_1(B, C, N)_1$
$Fe_4(C,N)$	FE4N_LP1	cP5	$Pm\bar{3}m$	221	$(Co, Cr, Fe, Mn, Ni)_4(C, N)_1$
$M_{23}C_6$	M23C6_D84	cF116	$Fm\bar{3}m$	225	$(Co, Cr, Fe, Mn, Ni, V)_{20}$ $(Co, Cr, Fe, Mn, Mo, Ni, V,W)_3 (B, C)_6$
M_6C	M6C_E93	cF112	$Fd\bar{3}m$	227	$(Co, Fe, Ni)_2(Mo, W)_2$ $(Co, Cr, Fe, Mo, Ni, Si, V,W)_2C_1$
Hexagonal precipitates					
M_2C (HCP)	HCP_A3#N*	hP2	$P6_3/mmc$	194	$(Al, Co, Cr, Cu, Fe, Mn, Mo, Ni, S, Si, Ti, V, W)_1(B, C, N)_{0.5}$
MC η	MC_ETA	hP12	$P6_3/mmc$	194	$(Mo, Ti, V, W)_1C_1$
MC shp	MC_SHP	hP2	$P\bar{6}m2$	187	$(Mo, W)_1(C, N)_1$
Monoclinic precipitates					
KSI carbide	KSI_CARBIDE	mS44	C2/m	12	$(Cr, Fe, Mo, W)_3C_1$
M_5C_2 (Hägg carbide)	M5C2	mS28	C2/c	15	$(Fe, Mn, Nb, V)_5(C, N)_2$

*where N is a number 1 through N number of phases of that crystal structure present in the system

The lattice parameters as a function of temperature and composition for the precipitates of interest are extracted from the molar volumes. This is the molar volume at equilibrium, which may not be the exact same composition as what would be kinetically favored to precipitate; however, determining the kinetically favored composition is much less amenable to high-throughput calculations. Figure 7 shows the variation in molar volume for the 12 carbides of interest calculated for a broad composition range of martensitic steels (~250 different alloy compositions plus a range of temperatures[10]). Some phases, such as $Fe_4(C,N)$, KSI carbide, and M_3C_2, clearly exhibit a narrow range of lattice parameters regardless of composition and temperature. Others span a wide range of molar volumes, particularly the FCC and HCP carbides.

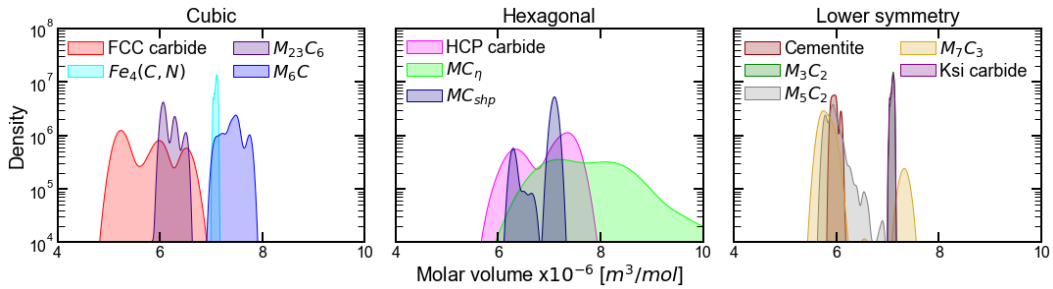

Figure 7. Variation in equilibrium molar volume for the 12 most common precipitates in steels from the THOMAS dataset.[10]

To convert from molar volume to meaningful lattice parameters, we use the number of atoms per unit cell,

$$VM\ \left[\frac{m^3}{mol}\right]\left(\frac{mol}{N_{AV}}\right)\left(\frac{10^{-10}\text{Å}}{m}\right)^3\left(\frac{atoms}{unit\ cell}\right) \rightarrow V_{cell}\ [\text{Å}]\,, \tag{4}$$

and then, information about the crystallography of the unit cell to derive the lattice parameters. The general formula for cell volume as a function of lattice parameters is

$$V_{cell} = a\,b\,c\,\sqrt{1-\cos^2\alpha-\cos^2\beta-\cos^2\gamma+2\cos\alpha\cos\beta\cos\gamma}\,, \tag{5}$$

where the lattice parameters are a, b, c, and the cell angles are α, β, γ. Crystallographic symmetry considerably reduces Equation 5, e.g., for cubic carbides, where $a=b=c$, and $\alpha=\beta=\gamma=90$ *degrees* the lattice parameter is simply $a = \left(V_{cell}\ [\text{Å}]\right)^{1/3}$. The angles and reduced cell volume equations are shown in Table 3.

Table 3. Crystallographic information for cell volume calculation. Angles from Jain et al.[32]

Crystal structure	α	β	γ	V_{cell}
Cubic	90	90	90	a^3
Hexagonal	90	90	120	$a^2c\sin(60)$
Orthorhombic	90	90	90	abc
Monoclinic				$abc\sin(\beta)$
M_5C_2	90	97.5	90	
KSI	90	120.7	90	

To determine the lattice parameters of the noncubic crystal structures directly from the unit cell volume, we require a relationship between the lattice parameters, i.e., the ratios a:c and a:b. Using cementite (orthorhombic) as an example, literature values for the lattice parameters of cementite with various compositions are tabulated in Table 4 with experimentally measured values in italics. The ratios of c:a and b:a are fairly consistent across different compositions and measurements

with values of approximately 0.88 and 1.33, respectively. Using these ratios in Equation 5 in conjunction with the molar volume from Thermo-Calc for the cementite precipitates in the dataset of approximately 2000 alloy temper combinations, the lattice parameters as a function of composition (Figure 8) and temperature (Figure 9) can be discerned. There is excellent agreement between the average literature lattice parameter, *a*, of 5.091 Å and the average *a* of 5.138 Å (5.131 Å stable/5.153 Å metastable) calculated from Thermo-Calc, even given the assumptions made.

Table 4. Elastic and lattice parameters from literature for cementite (M_3C).

Phase	Ref.	G_{Hill} [GPa]	ν	a [Å]	b [Å]	c [Å]	c:a	b:a
	[34]	. . .	. . .	*5.089*	*6.743*	*4.524*	0.889	1.33
	[35]	119.63	0.30	. . .	. . .	. . .	. . .	. . .
	[36]	55.97	0.37	5.09	6.67	4.47	0.878	1.31
	[36]	97.86	0.31	5.07	6.45	4.47	0.882	1.27
	[26, 27]	67.34	0.36	5.029	6.72	4.48	0.891	1.34
Fe_3C	[27]	*74.00*	*0.36*	. . .	. . .	. . .	. . .	. . .
	[27]	*70.00*	*0.26*	. . .	. . .	. . .	. . .	. . .
	[27]	*69.00*	*0.23*	. . .	. . .	. . .	. . .	. . .
	[27]	*72.00*	*0.26*	. . .	. . .	. . .	. . .	. . .
	[27]	*72.00*	*0.32*	. . .	. . .	. . .	. . .	. . .
	[27]	*90.00*	*0.27*	. . .	. . .	. . .	. . .	. . .
Fe_2MnC	[33]	92.08	0.25	5.135	6.646	4.472	0.871	1.29
Fe_2CrC	[26, 27]	76.93	0.35	5.02	6.82	4.38	0.873	1.36
Fe_2CrC	[33]	88.54	0.29	5.020	6.861	4.391	0.875	1.37
Fe_2CoC	[26]	. . .	. . .	4.99	6.68	4.49	0.900	1.34
Fe_2VC	[26]	. . .	. . .	5.10	6.68	4.53	0.888	1.31
$(Fe,Mn)_3C$	[34]	. . .	. . .	*5.04*	*6.73*	*4.51*	0.895	1.34
$(Fe,Cr)_3C$	[34]	. . .	. . .	*5.062–5.075*	*6.714–6.711*	*4.504–4.512*	0.889	1.32
Fe-based		**80.41**	**0.30**					
	[26, 27]	135.22	0.31	5.22	6.79	4.26	0.816	1.30
	[26]	. . .	. . .	*5.11*	*6.76*	*4.53*	0.886	1.32
Mn_3C	[26]	. . .	. . .	*5.10*	*6.79*	*4.55*	0.892	1.33
	[26]	. . .	. . .	*5.08*	*6.77*	*4.53*	0.892	1.33
	[34]	. . .	. . .	*5.080*	*6.772*	*4.53*	0.892	1.33
$FeMn_2C$	[33]	88.80	0.36	5.005	6.704	4.449	0.889	1.34
$FeMn_2C$	[26]	. . .	. . .	4.97	6.46	4.42	0.889	1.30
Mn-based		**112.01**	**0.335**					
Cr_3C	[26, 27]	139.95	0.29	5.19	6.62	4.511	0.869	1.28
	[26]	. . .	. . .	*5.12*	*6.80*	*4.58*	0.895	1.33
	[35]	137.70	0.30	. . .	. . .	. . .	. . .	. . .
	[37]	146.8	0.28	5.188	6.667	4.521	0.871	1.29
$FeCr_2C$	[33]	137.77	0.28	5.0997	6.604	4.524	0.887	1.30
$FeCr_2C$	[26, 27]	138.22	0.30	5.12	6.55	4.52	0.883	1.28
Cr-based		**140.09**	**0.29**					
Co_3C	[26, 27]	94.99	0.33	4.94	6.70	4.43	0.897	1.36
Co_3C	[34]	. . .	. . .	*5.033*	*6.731*	*4.483*	0.891	1.34
$FeCo_2C$	[26]	. . .	. . .	4.93	6.81	4.44	0.901	1.38
V_3C	[26, 27]	100.35	0.29	5.63	7.88	4.19	0.744	1.40
FeV_2C	[26]	. . .	. . .	5.09	6.80	4.71	0.925	1.34
M_3C				**5.091**			**0.880**	**1.33**

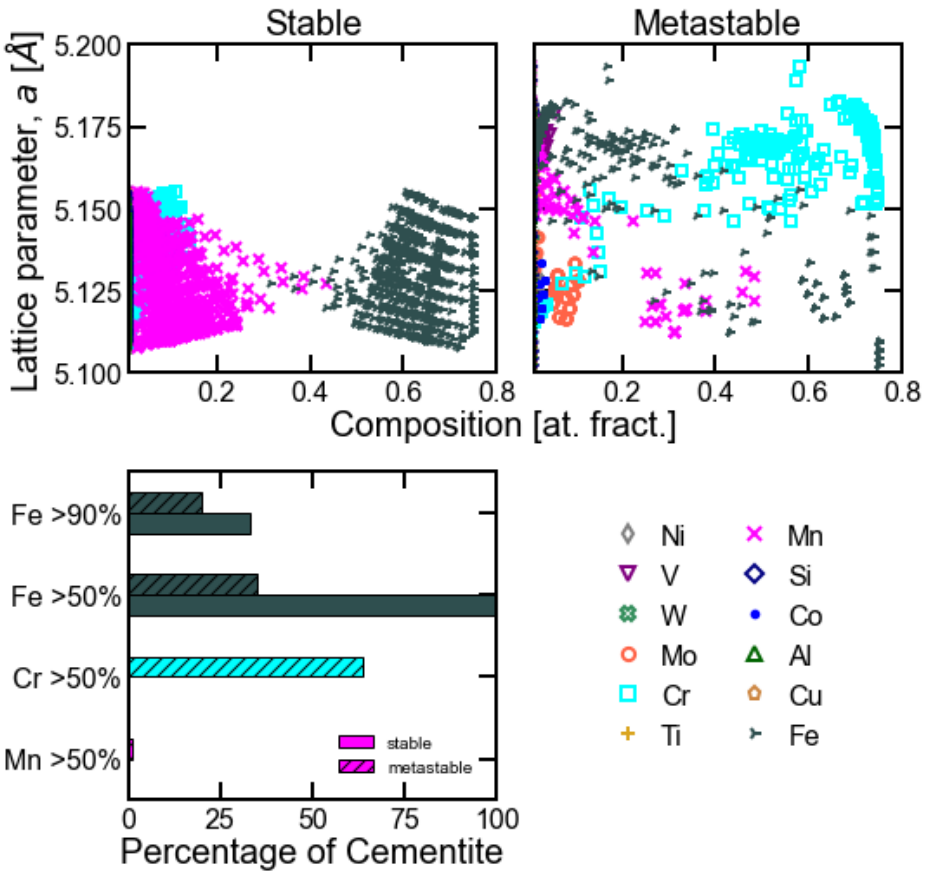

Figure 8. Compositions of stable and metastable cementite (Fe_3C) phases predicted from Thermo-Calc and corresponding lattice parameters calculated using the average lattice ratios at the bottom of Table 4 and 16 atoms/unit cell.[32]

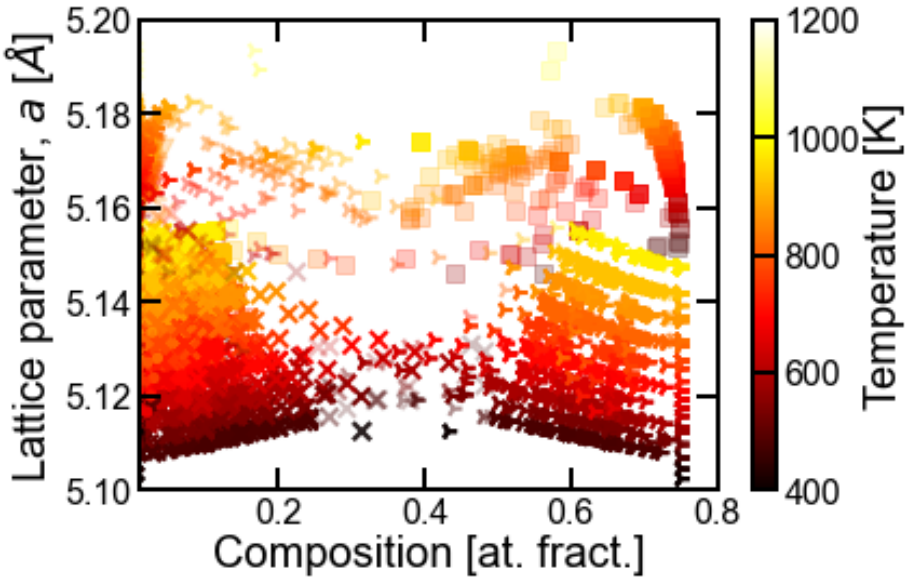

Figure 9. Cementite phases from Thermo-Calc as a function of temperature. Plot symbols correspond to the elements in Figure 8 and are colored by temperature.

From Figure 8, the stable cementite phases are Fe_3C with some substitution of Mn and Cr as expected. Including metastable phases, some Cr-rich $(Cr, Fe)_3C$ are also present; still, 85% of the possible (stable and metastable) cementite phases are majority Fe (i.e., of the 0.75 in the phase that is M, >50% is Fe). While the variation in lattice parameter for the cementite phase is not large overall (<2%), it can still be seen that increasing Mn content shrinks the lattice parameter while Cr increases it. This is consistent with literature values.[26,27,33] There is also a minor role of temperature on the lattice parameter (Figure 9), where lattice parameter increases with temperature as expected. It should be noted that many of the literature lattice parameters are from DFT studies, which would be at extremely low temperatures. Hence the fact that the calculated *a* is higher than literature *a* is not surprising when taking temperature into account.

It can be seen from Table 4 that, while the lattice parameter is not strongly affected by the composition of the phase, the shear modulus is different between Fe_3C and alloyed cementite. Both Cr and Mn increase the shear modulus relative to Fe_3C. Therefore, we aggregate the shear moduli and Poisson's ratio are based on the majority compositional element.

Next, we examine an example of a precipitate with a wide range of molar volumes (Figure 7), the FCC carbide phase, MC.

There are about 900 primary FCC carbides predicted across the combination of alloys and tempers in the dataset. The compositions and lattice parameters of the phases are shown in Figure 10, distinguished by stable and metastable carbides. The FCC carbides are partitioned based upon majority element. In Figure 10, the results of this partition between the five possible majority elements (Cr, V, Ti, Mo, and Mn) are shown as a bar chart for both stable and metastable phases. The stable FCC carbides are primarily TiC, VC, and CrC. The CrC have Mn solubility, i.e., (Cr,Mn)C, and the VC have some Fe and Cr solubility, i.e., (V, Fe, Cr)C. The lattice parameters for the average literature values of TiC, VC, and CrC from Table 5 are shown in Figure 10. The lattice parameter of TiC > VC > CrC is as expected. The average calculated *a* of 4.24 Å is again in good agreement with the average literature value of 4.17 Å. The effect of temperature on the lattice parameter of the MC carbides is shown in Figure 11. The lattice parameter of VC is strongly dependent on temperature compared to the CrC and TiC.

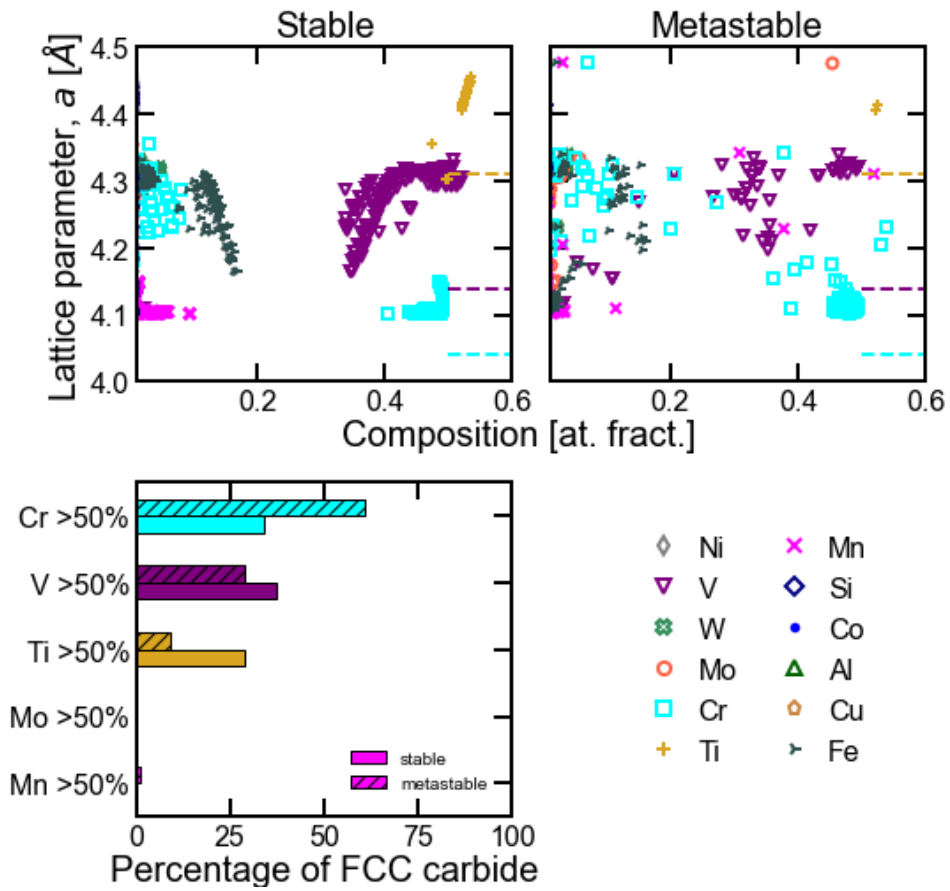

Note: Dashed lines are average literature lattice parameters for TiC, VC, and CrC

Figure 10. Compositions of stable and metastable FCC carbides (MC) phases predicted from Thermo-Calc and corresponding lattice parameters calculated using eight atoms/unit cell.[32]

Table 5. Elastic and lattice parameters from literature for FCC carbides.

Phase	Ref.	G_{Hill} [GPa]	ν	a=b=c [Å]
TiC	[34]	. . .	. . .	*4.296–4.326*
	[38]	200.16	0.21	4.2744
	[38]	179.98	0.21	4.3491
	[38]	187.80	0.21	. . .
	[38]	168.34	0.25	. . .
	[38]	173.79	0.21	. . .
	[39]	179.00	0.21	4.317
Ti-based		**181.51**	**0.217**	
VC	[34]	. . .	. . .	*4.118–4.165*
	[38]	247.88	0.21	4.1029
	[38]	222.28	0.21	4.1694
	[40]	223.61	0.24	4.156
	[40]	191.06	0.25	4.159
	[40]	. . .	. . .	4.163
V-based		**221.21**	**0.228**	
CrC	[34]	. . .	. . .	*3.62*
	[38]	178.00	0.30	4.0085
	[38]	161.67	0.29	4.076
	[38]	188.40	0.28	. . .
	[38]	156.30	0.31	. . .
	[37]	156.28	0.31	4.068
	[41]	163.49	0.3	4.08
	[41]	. . .	. . .	*4.03*
	[41]	. . .	. . .	*4.01*
Cr-based		**167.36**	**0.30**	
MoC	[41]	161.80	0.30	4.388
	[42]	152.20	0.32	4.36
	[38]	165.57	0.29	4.3719
	[38]	188.27	0.29	4.3215
Mo-based		**166.96**	**0.30**	
W_2C	[34]	. . .	. . .	4.222
				4.17

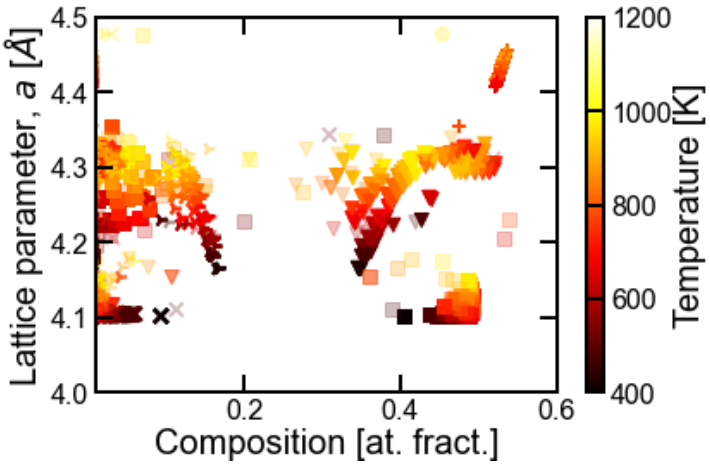

Figure 11. Composition of FCC carbides (MC) as a function of temperature. Plot symbols correspond to the elements in Figure 10 and are colored by temperature.

Plotting the elastic properties as a function of lattice parameter and primary element (Figure 12), it is clear that the composition is the dominant factor. Therefore, we will assign a shear modulus and Poisson's ratio for a given FCC carbide by composition, calculated as an average from the values in Table 5. For the rare cases in which the primary element in the FCC carbide is not one of the main four, an average value of all compositions will be used.

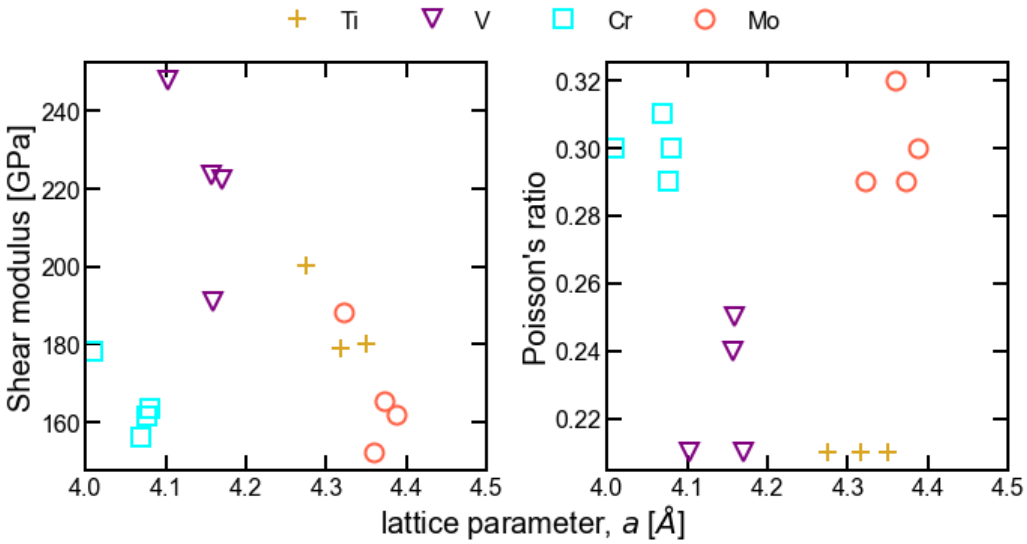

Figure 12. Trends in shear modulus and Poisson's ratio as a function of lattice parameter and composition for FCC carbides in Table 5.

The details of the remaining 10 carbides are compiled in Appendix B; the summary of all lattice parameter calculations is shown in Table 6.

The average value of the lattice parameter *a* based on the molar volume calculation from Thermo-Calc (Avg. *a* T-C) is compared to the average value of this lattice parameter based on literature values from the sections below (Avg. *a* LIT) and found to be in excellent agreement across all 12 carbides. Thus, we have confidence in using this approach to calculate the lattice parameters for the interfacial energy calculations. The use of the molar volume from Thermo-Calc calculations to derive the lattice parameter (as a function of temperature and composition) for each precipitate enables high throughput calculations and satisfies one of the four necessary inputs for the interfacial energy calculation.

Table 6. Volume structure of precipitate phases.

Phase	Avg. VM $\left[\frac{m^3}{mol}\right]\times 10^{-6}$	No. of atoms/ unit cell [Ref. 32]	Avg. V_{cell} [Å^3]	c:a (b:a) ratio	Avg. a TC [Å]	Avg. a LIT [Å]
Cubic						
FCC carbide (MC)	5.75	8	76.39	1	4.24	4.17
$M_{23}C_6$	6.20	116	1193.5	1	10.607	10.49
M_6C	7.42	112	1379.5	1	11.131	11.13
$Fe_4(C, N)$	7.10	5	47.13	1	3.612	3.75
Hexagonal						
HCP carbide (M_2C)	6.98	3[a]	34.76[a]	1.58	2.938	2.952
MC η (hP12)[b]	8.69	33[a,b]	476.1[a,b]	2.81[b]	5.427[c]	5.068[b]
MC shp (hP2)	7.01	2[a]	23.29[a]	0.971	3.025	2.912
Orthorhombic						
Cementite M_3C	5.97	16	158.7	0.880 (1.33)	5.138	5.091
M_3C_2	7.10	20	235.8	2.08 (0.51)	6.057	5.512
M_7C_3	5.89	40	391.4	2.65 (1.53)	4.586	4.49
Monoclinic						
M_5C_2	5.95	28	276.6	0.44 (0.397)	11.69	11.202
KSI	7.10	44	518.4	0.6 (0.71)	11.228	10.865

[a] For primitive cell of hexagonal prism
[b] Assuming V_6C_5
[c] Average of stable MCη only

As shown in the two illustrative examples, the necessary elastic constants can be pulled from literature and often show trends by composition. However, this is not truly a high-throughput solution. Therefore, an attempt was made to pull elastic constants from the Materials Project[32]; however, only about half of the precipitates of interest have elastic constants in the database (see Table 7). Further, several extracted elastic constants are obviously unphysical (e.g., negative elastic stiffness values) indicated by red shading in Table 7. Others deviate by greater than 10% from literature values from studies specifically on the phase (indicated by yellow shading). Consequently, it is not currently a viable method for collection of elastic properties—high-throughput or otherwise.

Table 7. Mechanical property values extracted using the materials project application programming interface.

Phase	Materials project ID no.	G_{Voight}	G_{Reuss}	G_{VRH}	Poisson's ratio	a	b	c
TiC	631	173	172	172	0.22	4.33	4.33	4.33
VC	1282	211	206	209	0.22	4.16	4.16	4.16
CrC	579	106	87	96	0.16	4.11	4.11	4.11
MoC	2746	196	184	190	0.26	4.38	4.38	4.38
$Cr_{23}C_6$	723	–2334769	175	–1167297	0.25	10.49	10.49	10.49
$Fe_{23}C_6$	1192884	. . .	. . .	. . .	. . .	10.45	10.45	10.45
$Mn_{23}C_6$	542830	. . .	. . .	. . .	. . .	10.5	10.5	10.5
Fe_3W_3C	20696	. . .	. . .	. . .	. . .	11.08	11.08	11.08
Co_3W_3C	1192636	. . .	. . .	. . .	. . .	11.1	11.1	11.1
Ni_3W_3C	1194387	. . .	. . .	. . .	. . .	11.09	11.09	11.09
Fe_3Mo_3C	1193060	. . .	. . .	. . .	. . .	11.06	11.06	11.06
Fe_4C	1246	–48	–41	–44	0.65	3.84	3.84	3.84
Mo_2C	571589	–516	40	–238	1.31	2.88	2.88	5.49
V_2C	1008632	120	80	100	0.3	2.88	2.88	4.5
Cr_2C	1226378	…	…	…	…	2.82	2.82	4.23
W_2C	1008625	161	150	156	0.29	3.07	3.07	4.68
MoC	2305	244	239	242	0.22	2.91	2.91	2.82
WC	1894	269	257	263	0.22	2.92	2.92	2.84
V_6C_5	28731	177	174	175	0.2	5.09	5.09	14.33
Cr_3C	1189286	. . .	. . .	. . .	. . .	4.47	5.19	6.59
Fe_3C	510623	93	44	68	0.36	4.49	5.03	6.74
Mn_3C	1188188	. . .	. . .	. . .	. . .	4.44	4.94	6.7
Co_3C	20925	. . .	. . .	. . .	. . .	4.43	4.94	6.7
Cr_3C_2	20937	176	160	168	0.28	2.79	5.44	11.39
Cr_7C_3	19855	. . .	. . .	. . .	. . .	4.48	6.9	11.94
Fe_7C_3	21717	. . .	. . .	. . .	. . .	4.52	6.86	11.76
Mn_7C_3	21256	. . .	. . .	. . .	. . .	4.46	6.81	11.7
Fe_5C_2	2794	100	75	88	0.33	11.6	4.51	4.99
KSI	571055	. . .	. . .	. . .	. . .	10.99	7.65	6.56

2.3.3 Summary of Elastic Parameters

We have detailed the derivation of the necessary materials parameters for two examples of the precipitate phases (with the remainder in Appendix B). The necessary elastic properties used for all precipitates are listed in Table 8. For the precipitate phases, the values are often based on the compositions; however, in some cases a single average value can be used for the phase. For one phase (M_6C), they are functions of lattice parameter.

Table 8. Final mechanical parameters for the 12 precipitates.

Phase	Thermo-Calc label	Shear modulus [GPa]	Poisson's ratio
		Orthorhombic	
M_3C (cementite)	CEMENTITE_D011	Cr: 140.09 Fe: 80.41	Cr: 0.29 Fe: 0.30
M_3C_2	M3C2_D510	Mn: 112.01 *182*	Mn: 0.335 *0.26*
M_7C_3	M7C3_D101	Mn: 103.6 Fe: 107.6 Cr: 119.6 Alloy: 138.4	Mn: 0.36 Fe: 0.33 Cr: 0.33 Alloy: 0.32
		Cubic	
MC (FCC carbides)	FCC_A1#2	Mo: 166.96 Cr: 167.36 V: 221.21 Ti: 181.51 Alloy: 184.26	Mo: 0.3 Cr: 0.3 V: 0.228 Ti: 0.217 Alloy: 0.26125
$Fe_4(C,N)$	FE4N_LP1	79.64	0.36
$M_{23}C_6$	M23C6_D84	137.5	0.329
M_6C	M6C_E93	for 11.5 > a > 10.8: $-126.9a + 1552.9$ else: 140.79	0.317
		Hexagonal	
M_2C (HCP carbides)	HCP_A3#2	149.71	0.27
MC η	MC_ETA	Mo: 160.81 V: 191.44 Alloy: 191.44	Mo: 0.29 V: 0.2 Alloy: 0.2
MC shp	MC_SHP	Mo: 232.99 W: 287.01	Mo: 0.2225 W: 0.2033
		Monoclinic	
KSI carbide	KSI_CARBIDE	71.51	0.367
M_5C_2 (Hagg carbide)	M5C2	Mn: 127.7 Fe: 107.9	Mn: 0.317 Fe: 0.337

2.4 Matrix

The compositions and lattice parameters of the matrix phase for the alloys and temperatures in the dataset are shown in Figure 13. The lattice parameter increases with temperature as expected while the composition only has a minor effect; in all, the lattice parameter is static with only an approximately 1% change.

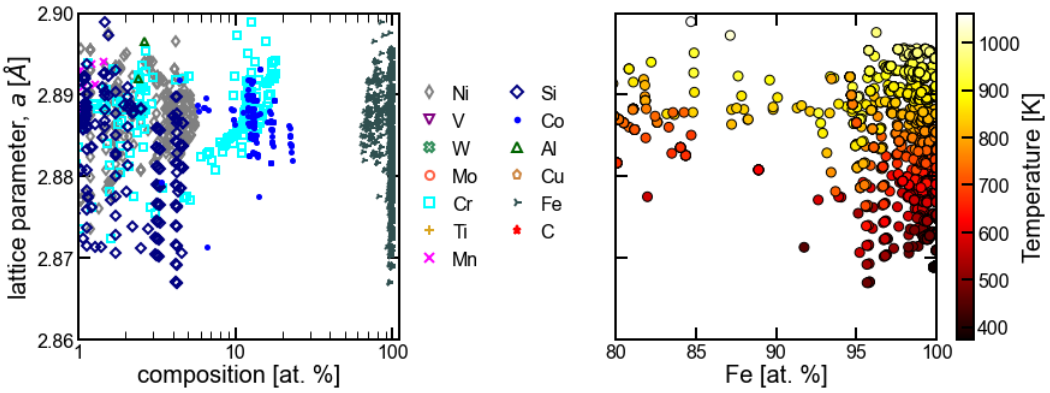

Figure 13. Lattice parameter as a function of matrix composition and temperature.

As mentioned previously, for the matrix phase we consider the effects of temperature on the elastic properties. The shear modulus as a function of temperature for α-martensite was derived in Ghosh and Olson[30]:

$$G_{\alpha'} = \left(8.068 + \sum x_j \left(\frac{d\mu}{dx_j}\right)_{Total}\right)\left[1 - 0.48797\left(\frac{T}{T_C}\right)^2 + 0.12651\left(\frac{T}{T_C}\right)^3\right] x10^{10}\ Pa\ for\ T < T_C \quad (6)$$

where T is the temperature and T_C is the Curie temperature. Alloying effects are incorporated through the $d\mu/dx$ term with the coefficients in Table 9. In the original work,[30] the Curie temperature was also a function of alloy content and was obtained using a thermodynamic database (kMART[43]). The Curie temperatures for the approximately 2000 matrix compositions in this dataset were pulled from Thermo-Calc TCFE10 database and their distribution is shown in Figure 14a. The T_C for most compositions center around 1043 K (dashed line), the T_C for pure Fe. There is also a subset where TCFE10 predicts the matrix is antiferromagnetic rather than ferromagnetic and returns a Néel temperature, shown by the peak below 200 K. One solution would be to assume 1043 K for the T_C in cases where a Néel temperature is returned, to calculate the shear modulus via Equation 6; another is to just use 1043 K for all the compositions—this is also more in line with maintaining high-throughput calculations, as it eliminates the call to the Thermo-Calc database to obtain the composition-dependent T_C. Figure 14b shows the difference between calculating the shear modulus using the composition-dependent T_C and the pure Fe T_C. There is at most a 6.8% difference in the shear modulus, and only an average of 0.73% (median of 0.36%) difference; the difference does increase with the tempering temperature. The two maximum difference alloys are tempered at temperatures over their Curie temperature, leading to the high differential. The cluster in the middle (~5%, 65 GPa) are maraging steels, which

have a very high alloy content and low carbon content, depressing the predicted T_C considerably.

Table 9. Coefficients for calculation of shear modulus using Equation 6 for α-martensite from Ghosh and Olson.[30]

Element	$(d\mu/dx_j)_{Total}$ ($\times 10^{10}$ N/m^2)
Al	–10.085
C	–14.194
Co	2.389
Cr	3.406
Cu	–0.145
Mn	–2.263
Mo	–1.671
N	–15.439
Nb	–8.707
Ni	–9.065
Si	–10.914
Ti	–7.459
V	1.014
W	7.267

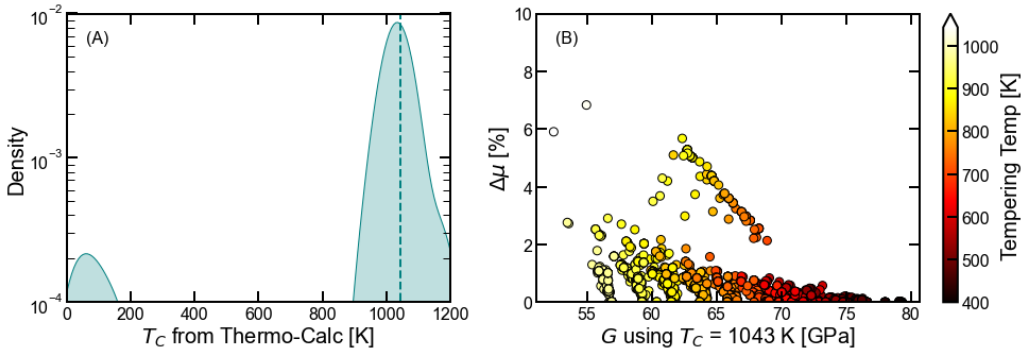

a) b)

Figure 14. a) Distribution of Curie temperatures (dashed line is 1043 K pure Fe); b) effect on shear modulus using 1043 vs. alloy-specific TC (ones with Neel are excluded).

The Poisson's ratio as a function of temperature and composition for the matrix phase is derived from the shear and bulk moduli, where the shear modulus is calculated from Equation 6, and the bulk modulus is from Ghosh and Olson[30]:

$$B_{\alpha-Fe} = 17.187\left[1 - 0.28029\left(\frac{T}{T_C}\right)^2 + 0.07221\left(\frac{T}{T_C}\right)^3\right] x10^{10}\ Pa\ for\ T < T_C \quad (7)$$

Poisson's ratio is then calculated as:

$$\nu = \frac{3B_{\alpha-Fe} - 2G_{\alpha\prime}}{2(3B_{\alpha-Fe} + G_{\alpha\prime})} \quad (8)$$

Poisson's ratio does not vary much with temperature or composition.

2.5 Orientation Relationships (ORs)

Given the materials' properties of both the precipitate and the matrix, the calculation is then performed as a function of OR. Table 10 lists the ORs used in this work for the precipitates in a ferrite/martensite matrix as a function of precipitate crystal structure. This is not an exhaustive list, for example, it only includes the two main ORs of cementite and not all the twist angles,[36] as it is intended to illustrate that there can be variations in energy as a function of OR. Each OR is defined by a shared interface plane expressed in local crystallographic coordinates as well as two sets of parallel vectors within the interface plane.

Several ORs are commonly observed across various precipitate and matrix materials while others are very specific to the precise crystallographic structure at hand. It was found that the reported ORs for the Hagg carbide (M_5C_2)[44] were functionally the same as the Bagaryatski OR for cementite, so that was used in this work (Table 10). The *c* planes of cementite and M_5C_2 are shown in Figure 15a. Among the considered precipitates, ORs for one that could not be found in literature is the monoclinic KSI carbide ($M_{17}C_5$). Therefore, an OR is proposed here, though includes comparison with similar crystal structures and analysis of relevant distances and angles between atoms. The KSI carbide has no apparent analog to other ORs and so it was necessary to inspect atomic positions to identify potential O-lattice sites. Starting with the highest symmetry direction and most likely Burgers vector within the ferrite of [111], planes were searched within the KSI carbide in which the bond angles closely matched the angles within this family of ferrite crystallographic directions. The *c* planes within the KSI carbide match well, with bond angles of approximately 69.66° matching almost identically with the 70.53° found in the ferrite between the *a/2*[111] directions, as seen in Figure 15b.

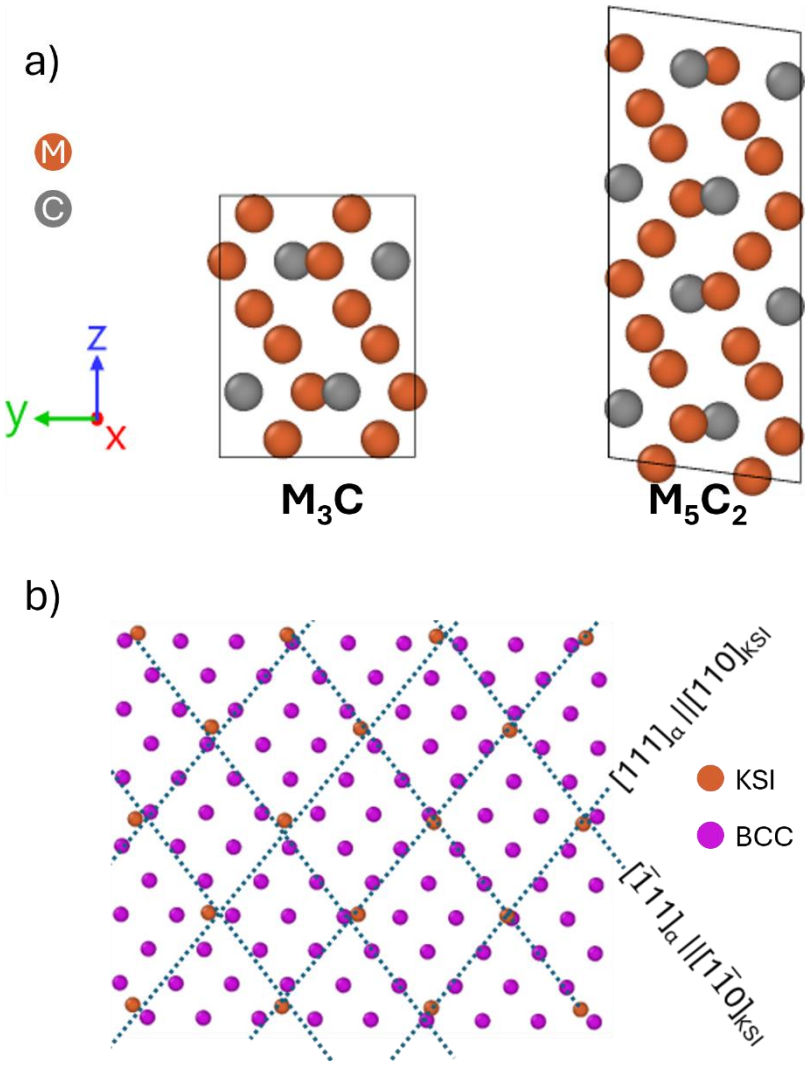

Figure 15. a) The *c* planes for cementite M_3C and Hagg carbide M_5C_2 showing the similarity and b) interface plane for KSI carbide (magenta) and ferrite matrix (orange) with OR indicated.

Table 10. ORs between precipitate and BCC matrix.

OR [Refs.]	Precipitate // Matrix	Precipitate	Cell ratios
Bain (Baker–Nutting) [34, 45, 46]	$[110]//[010]_\alpha$ $[100]//[110]_\alpha$ $(001)//(001)_\alpha$	MC (FCC) $Fe_4(C,N)$ $M_{23}C_6$ M_6C	$a_{MC} : a_{BCC}$ $a_{Fe4(C,N)} : a_{BCC}$ $a_{M23C6} : 3\ a_{BCC}$ $a_{M6C} : 3\ a_{BCC}$
Kurdjumov–Sachs [47, 48]	$[10\bar{1}]//[11\bar{1}]_\alpha$ $[0\bar{1}1]//[1\bar{1}1]_\alpha$ $(111)//(011)_\alpha$	MC (FCC) $Fe_4(C,N)$ $M_{23}C_6$ M_6C	$a_{MC} : a_{BCC}$ $a_{Fe4(C,N)} : a_{BCC}$ $a_{M23C6} : 3\ a_{BCC}$ $a_{M6C} : 3\ a_{BCC}$
Nishiyama–Wasserman [48]	$[\bar{1}10]//[\bar{1}00]_\alpha$ $[11\bar{2}]//[01\bar{1}]_\alpha$ $(111)//(011)_\alpha$	MC (FCC) $Fe_4(C,N)$ $M_{23}C_6$ M_6C	$a_{MC} : a_{BCC}$ $a_{Fe4(C,N)} : a_{BCC}$ $a_{M23C6} : 3\ a_{BCC}$ $a_{M6C} : 3\ a_{BCC}$
Pitsch [49]	$[01\bar{1}]//[11\bar{1}]_\alpha$ $[0\bar{1}1]//[1\bar{1}1]_\alpha$ $(100)//(011)_\alpha$	MC (FCC) $Fe_4(C,N)$ $M_{23}C_6$ M_6C	$a_{MC} : a_{BCC}$ $a_{Fe4(C,N)} : a_{BCC}$ $a_{M23C6} : 3\ a_{BCC}$ $a_{M6C} : 3\ a_{BCC}$
Pitsch–Schrader [34, 50]	$[1\bar{1}00]//[1\bar{1}0]_\alpha$ $[1\bar{2}10]//[1\bar{1}1]_\alpha$ $(0001)//(110)_\alpha$	M_2C MC (SHP) MC (η)	$a_{M2C} : a_{BCC}$ $a_{MC\_SHP} : a_{BCC}$ $a_{MC\_ETA} : \sqrt{3}\ a_{BCC}$
Burgers [48]	$[11\bar{2}0]//[1\bar{1}1]_\alpha$ $[\bar{2}110]//[11\bar{1}]_\alpha$ $(0001)//(011)_\alpha$	M_2C MC (SHP)	$a_{M2C} : a_{BCC}$ $a_{MC\_SHP} : a_{BCC}$
Bagaryatski [36, 44, 48]	$[010]//[111]_\alpha$ $[100]//[1\bar{1}0]_\alpha$ $(00\bar{1})//(11\bar{2})_\alpha$	Fe_3C M_3C_2 M_7C_3 M_5C_2	$a_{Fe3C} : a_{BCC}$ $c_{Fe3C} : a_{BCC}$ $a_{M3C2} : a_{BCC}$ $3\ c_{M3C2} : 2\ a_{BCC}$ $2\ a_{M7C3} : 3\ a_{BCC}$ $c_{M7C3} : a_{BCC}$ $a_{M5C2} : a_{BCC}$ $c_{M5C2} : a_{BCC}$
Isaichev [36]	$[010]//[111]_\alpha$ $[\bar{1}0\bar{1}]//[0\bar{1}1]_\alpha$ $(\bar{1}01)//(2\bar{1}\bar{1})_\alpha$	Fe_3C M_3C_2 M_7C_3	$a_{Fe3C} : a_{BCC}$ $c_{Fe3C} : 2\ a_{BCC}$ $a_{M3C2} : a_{BCC}$ $c_{M3C2} : 3\ a_{BCC}$ $2\ a_{M7C3} : 3\ a_{BCC}$ $c_{M7C3} : 3\ a_{BCC}$
Monoclinic (KSI) [this work]	$[010]//[100]_\alpha$ $[100]//[011]_\alpha$ $(00\bar{1})//(0\bar{1}1)\alpha$	KSI carbide	$a_{KSI} : 3\ a_{BCC}$

Many of the precipitate phases examined are comprised of multiple subcells. In addition to the OR definitions listed in Table 10, the number of subcells per unit cell in the interface plane must be considered. These cell ratios are also listed in the last column of Table 10. As an initial example, simple cubic lattices such as FCC and Fe_4N map one-to-one to the BCC matrix. However, the more complex cubic lattices ($M_{23}C_6$ and M_6C) consist of three subcells within the interface plane and

therefore map as one-to-three to the BCC matrix lattice. Specifically, for $M_{23}C_6$ and M_6C, a_{FCC}:$3a_{BCC}$.

The even more complex orthorhombic lattices require up to two independent scaling factors with respect to the BCC lattice since there are potentially two unique principal lattice lengths in the interface plane. The Fe_3C in the Bagaryatski OR most closely maps directly to the BCC lattice. Along directions $[010]||[111]\alpha$, the mapping is one-to-one and along directions $[100]||[1\bar{1}0]\alpha$, the mapping is also one-to-one. An example of the Bagaryatski OR is shown in Figure 16. The Fe_3C in the Isaichev OR, however, does not directly map to the BCC lattice. Along directions $[010]||[111]\alpha$, the mapping is one-to-one; however, along directions $[\bar{1}0\bar{1}]||[0\bar{1}1]\alpha$, the mapping is one-to-two, i.e., a_{Ortho}:$2a_{BCC}$. This is illustrated in Figure 16 with the two BCC lattice units highlighted with blue dashed lines.

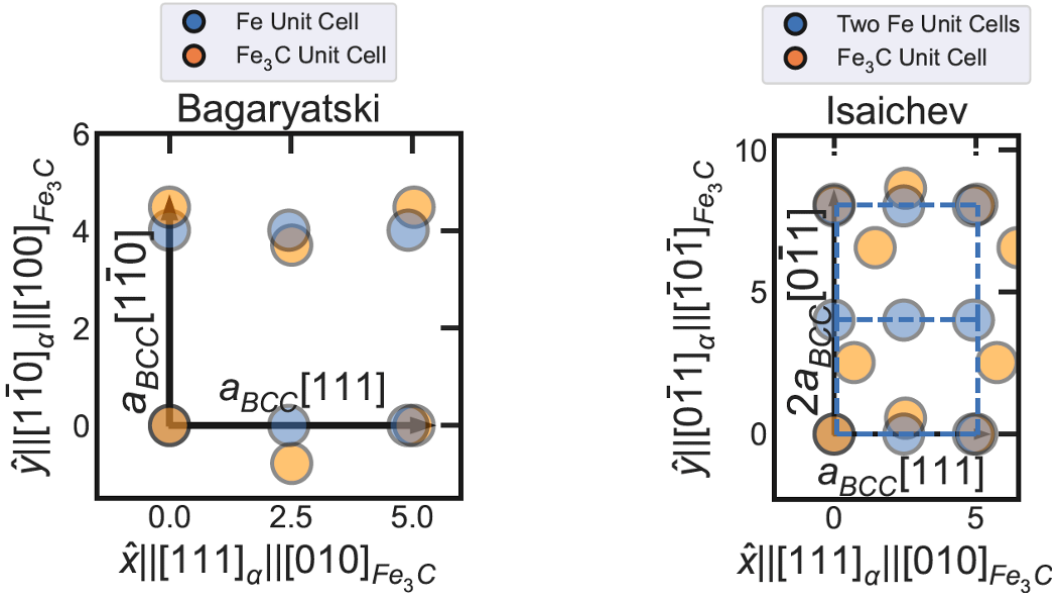

Figure 16. Orthorhombic ORs joining BCC lattice (blue) to Fe_3C lattice (orange). Bagaryatski OR (left) with one-to-one mapping between Fe and Fe_3C unit cells compared to Isaichev OR (right) with one-to-two mapping along the [0$\bar{1}$1] direction in the BCC lattice. The dashed box surrounds a unit Fe BCC cell.

3. Results

The elastic contribution to the interfacial energy is calculated for approximately 2000 combinations of alloys and temperatures using the 12 precipitate phases of interest and the possible ORs (for a total of 43,530 calculations). The lattice parameters are derived from Thermo-Calc as presented in Table 6. The elastic constants for the precipitates are summarized in Table 8 and for the matrix are represented by Equations 6 and 8. The ORs are described in Table 10.

The results of the elastic calculations are summarized in Figure 17. For precipitate-matrix interfaces with multiple ORs, the lowest energy OR is selected for the histogram in Figure 17. All calculations result in reasonable interfacial energy values (i.e., 0-1 J/m^2). Interestingly, the distribution of the elastic interfacial energy of several phases is much narrower than for the chemical contribution to interfacial energy (Figure 2, reproduced in Figure 18 with the TTT curve corrections). The narrowest distributions are those phases that have both a singular set of elastic parameters (e.g., not compositionally dependent) (see Table 8) and a narrow distribution of the lattice parameter. Critically, using realistic materials parameters for the carbide phases resulted in reasonable values for the elastic strain energy contribution to the interfacial energy. Future work will explore the sensitivity of the calculated elastic energy relative to the input materials parameters in more detail.

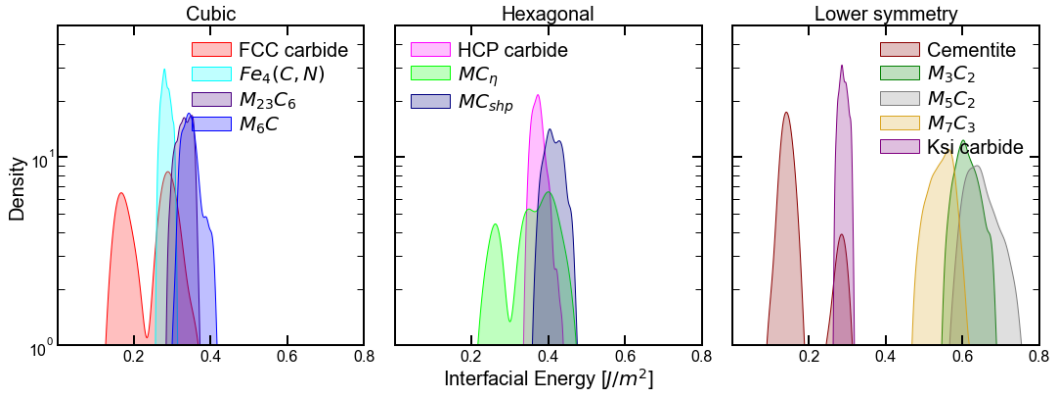

Figure 17. Calculated elastic interfacial energies.

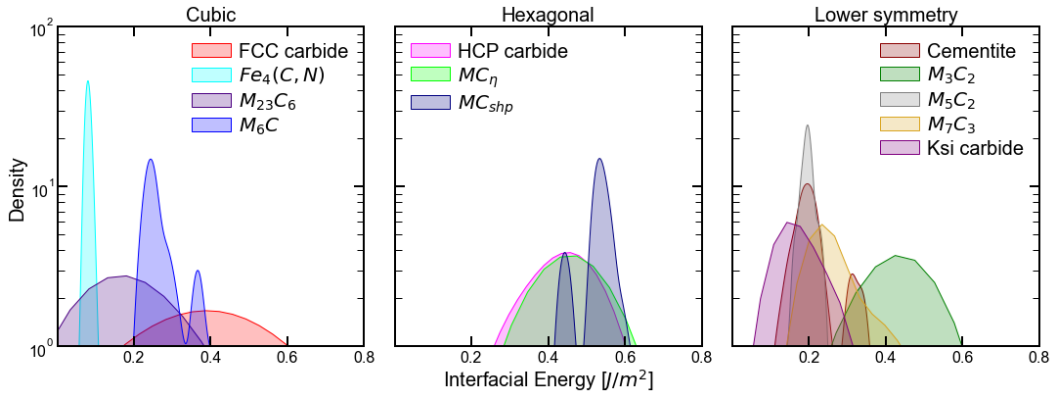

Figure 18. Chemical interfacial energy calculated from TTT curves.

Examining the values in more detail, the average interfacial energies for each carbide for both the elastic calculation, and the modified chemical calculation (TTT curve-based) are shown in Table 11. There is considerable improvement to the FCC carbides, where some are now coherent, and the remainder are semicoherent. The HCP carbides are still all semicoherent with none being coherent. A likely

explanation for this is that the generally observed coherent strengthening M_2C phases are nonequilibrium and may have evolving compositions with time. For example, in UHSS steels (i.e., AF1410, AerMet100), the Cr:Mo ratio is controlled to produce mixed M_2C carbides, $(Cr,Mo)_2C$, which have a lower lattice mismatch to the matrix than Mo_2C or Cr_2C[51] (Cr_2C hexagonal is semicoherent[52]). According to equilibrium calculations, which is what is presently used in this work, the composition of M_2C at the peak tempering temperature in AF1410 is Mo-rich. However, the nonequilibrium composition from precipitation calculations is about 2/3 Cr and 1/3 Mo; this is in line with experimental observations.[12] It can be seen in Appendix B (Figure B-6) that the Mo_2C are perhaps overrepresented, skewing the overall mismatch and subsequent elastic interfacial energy higher than would be observed experimentally. Using the equilibrium composition (as done here) is much faster from a computational standpoint when running Thermo-Calc but may not be the best choice for all phases.

Table 11. Average values of interfacial energy.

Precipitate	Coherency (in BCC matrix) [Ref. 14]	Avg calc. $\gamma_{elastic}$	Avg calc.[a] $\gamma_{chemical}$	$\gamma_{chemical} + \gamma_{elastic}$
Fe_3C	semi.	0.169	0.209	0.378
Fe_4N	semi.	0.285	0.067	0.351
FCC carbide (MC)	semi.	0.18/0.30 0.246	0.331	0.577
HCP carbide (M_2C)	semi.	0.376	0.353	0.730
M_7C_3	incoh.	0.549	0.269	0.818
$M_{23}C_6$	incoh.	0.331	0.181	0.512
M_6C	incoh.	0.351	0.282	0.633
KSI	. . .	0.290	0.174	0.464
MC_{SHP}	. . .	0.416	0.510	0.925
MC_η	. . .	0.355	0.459	0.814
M_5C_2	. . .	0.654	0.184	0.838
M_3C_2	. . .	0.613	0.427	1.04

[a] Using the TTT curve, not the default calculation

The two phases expected to be incoherent but predicted to be coherent by the chemical model—$M_{23}C_6$ and M_6C—have been greatly improved by the elastic model. For example, the interfacial energy of $M_{23}C_6$ was found to need a substantial increase from the Becker chemical model prediction to align with experimental results in Leitner et al.[15]; this is in line with the elastic predictions (Table 11).

Although these results are promising, there are still several assumptions inherent in the elastic calculations. These assumptions lead to sources of uncertainty. First, discrete dislocation theory includes a cutoff parameter on the order of one Burgers vector surrounding the dislocation core to circumvent divergent stress fields and energies (blue line, Figure 19). In this work, we use a nonsingular dislocation

theory, which behaves similarly to the singular model far from the dislocation core and converges to zero at the dislocation core. The nonsingular model leads to finite stresses and energies (Figure 19). However, the functional form for the stress field as it nears the dislocation core is phenomenological. It is parameterized by a core length scale (a), which is assumed to be one Burgers vector. This prescribed length scale parameterizes the dislocation stress fields near each dislocation core, which in turn influences the computed interface energy (Equation 3). While the assumption made for a in this work resulted in reasonable interfacial energy values, there are two main concerns in applying it across all precipitates as done here: 1) precipitates with lower dislocation spacings (higher dislocation density) at the interface are more affected by the assumption, as they are closer to the divergence near the dislocation core (Figure 19) and 2) as such, an explicit ranking of coherency across many precipitates at once may be affected.

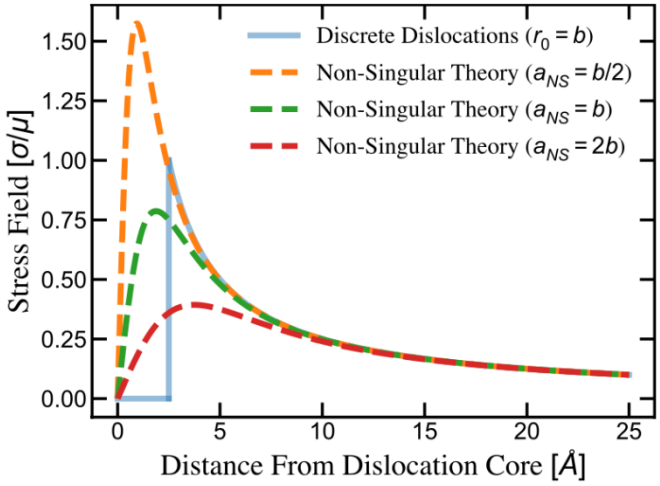

Figure 19. Example stress fields as a function of distance from dislocation core for several plausible dislocation core distributions.

If the goal is a precise interfacial energy, more sophisticated elastic models involving a refined treatment of the dislocation core are required. As an example, in other work using non-singular theory, the function near the dislocation core was explicitly fit to MD calculations.[53] This type of fitting procedure, however, while robust, can only be applied to a limited number of systems and is not amenable to high-throughput calculations.

To further investigate the influence of the dislocation core and isolate its contribution to the computed interface energy, we derived an asymptotic analytical model. This asymptotic model assumes that the dislocation core length scale is much smaller than $D_{1,2}$, and thus $\frac{a}{D_{1,2}} \ll 1$. The model explicitly expresses γ_{misfit}

as a function of Burgers vectors ($\boldsymbol{b}_i$), dislocation spacings (D_i) and the dislocation core length scale (a). Qualitatively, this model takes the form:

$$\gamma_{misfit} \approx A\frac{b_1^2}{D_1}\log\left(\frac{D_1}{a}\right) + B\frac{b_2^2}{D_2}\log\left(\frac{D_2}{a}\right) \quad (9)$$

where A and B are proportional to shear moduli. Several insights may be collected. First, note that the dislocation core length scale appears in a logarithm term; therefore, the influence over small ranges of $\frac{a}{D_{1,2}}$ is minimized relative to linear terms. Second, as noted, $\boldsymbol{b}_i/D_i$ are dislocation densities for each of two dislocation sets. Therefore, a decrease in dislocation density (increase in Di) leads to a decrease in the misfit energy, as to be expected intuitively. Third, if we ignore the dependence on $\log\left(\frac{D_{1,2}}{a}\right)$ and assume that $A \approx B$, it is easy to show that $\gamma_{misfit} \propto \frac{b_1^2 D_2 + b_2^2 D_1}{D_1 D_2}$. Since the area of each unit cell formed by dislocations is proportional to $D_1 D_2$, and the length is proportional to $D_1 + D_2$, the elastic interfacial energy may be viewed as a measure of surface dislocation density (dislocation length/area) required to form an interface between two otherwise dissimilar mismatched crystals. This surface dislocation density could be an alternate metric used to rank precipitates in a high-throughput fashion.

Another area necessitating further study is the sensitivity of the calculation to the precompiled materials parameters. The cell ratios determined from literature data obviously resulted in reasonable values for lattice parameters across the precipitates of interest (Table 6). However, it is likely that the ORs that involve multiple lattice parameters, *a* and *c*, whose values are related to each other through the compiled cell ratios, may be more sensitive to small changes in the ratio. Similarly, it is currently unclear how much the choice of representative average elastic parameters per phase affects the calculations. A sensitivity study is planned with respect to the material parameter inputs.

4. Conclusion and Future Work

We have demonstrated a high-throughput calculation of elastic interfacial energy requiring only four materials parameters, for greater than 40,000 combinations of carbides and ORs in a ferritic matrix.

For the materials parameters, a methodology was established to extract lattice parameters from the molar volume computed in Thermo-Calc with excellent agreement to experimental values. This enables high-throughput computation of lattice parameters as a function of temperature and composition for an arbitrary phase. The necessary elastic properties were collected for the carbides of interest

from literature sources; this process is somewhat laborious, but once a library is compiled, the elastic interfacial calculations themselves are rapid. Attempting to use the materials project library of elastic parameters to avoid the time-consuming literature search was found not to be feasible due to many missing or erroneous values. Similarly, with the ORs, a library of options is established prior to running the elastic calculations; this included determining likely ORs for a carbide phase where an OR could not be found in literature. Many phases have multiple possible ORs. In such cases, the elastic energy of each OR is calculated and the lowest energy identified as the elastic interfacial energy.

The predicted interfacial energies all fall within a reasonable range based on these assembled values for the materials parameters. Alignment between the results and expected coherency is good for many of the carbide/matrix combinations. We identified likely reasons for the discrepancies for other phases and the avenues for addressing the issues. These will be explored in a future work that also performs sensitivity analysis of the materials input parameters. We would like to determine the relative importance of variation in the elastic constants on the interfacial calculation due to the necessity of pre-compiling the dictionary of these values. Further, for future work we would like to incorporate full elastic anisotropy, i.e., considering the full stiffness/compliance matrix rather than just the shear modulus. We have already collected the full matrices where available although this work only reports the shear modulus.

A Python module containing the code necessary to execute the calculations is forthcoming and comprises a material agnostic class that uses a supplied-materials specific data structure with the values of Table 3 (crystallographic information necessary for lattice calculations), Table 10 (ORs), and Table 8 (elastic properties). This information can be compiled for different systems of interest while keeping the core calculation code unchanged.

5. References

1. Liu F, Xiao X, Huang L, Tan L, Liu Y. Design of NiCoCrAl eutectic high entropy alloys by combining machine learning with CALPHAD method. Mater Today Commun. 2022;30:103172. https://doi.org/10.1016/j.mtcomm.2022.103172

2. Peng J, Yamamoto Y, Hawk JA, Lara-Curzio E, Shin D. Coupling physics in machine learning to predict properties of high-temperatures alloys. NPJ Comput Mater. 2020:6(1):141. https://doi.org/10.1038/s41524-020-00407-2

3. Shen C et al. Physical metallurgy-guided machine learning and artificial intelligent design of ultrahigh-strength stainless steel. Acta Materialia. 2019;179:201–214. doi:10.1016/j.actamat.2019.08.033

4. Becker R. Die Keimbildung bei der Ausscheidung in metallischen Mischkristallen. Annalen der Physik. 1938;424(1–2):128–140. https://doi.org/10.1002/andp.19384240115

5. Meher S, Nag S, Tiley J, Goel A, Banerjee R. Coarsening kinetics of γ′ precipitates in cobalt-base alloys. Acta Materialia. 2013;61(11):4266–4276. https://doi.org/10.1016/j.actamat.2013.03.052

6. Devaux A et al. Gamma double prime precipitation kinetic in Alloy 718. Mater Sci Eng A. 2008;486(1–2):117–122. https://doi.org/10.1016/j.msea.2007.08.046

7. Noble B, Bray SE. Use of the Gibbs–Thompson relation to obtain the interfacial energy of δ′ precipitates in Al–Li alloys. Mater Sci Eng A. 1999;266(1–2):80–85. https://doi.org/10.1016/S0921-5093(99)00034-9

8. Zhang Q, Makineni SK, Allison JE, Zhao J-C. Effective evaluation of interfacial energy by matching precipitate sizes measured along a composition gradient with Kampmann-Wagner numerical (KWN) modeling. Scripta Materialia. 2019;160:70–74. https://doi.org/10.1016/J.SCRIPTAMAT.2018.09.048

9. Guziewski M, Coleman SP, Weinberger CR. Interface energetics and structure of the pearlitic microstructure in steels: an atomistic and continuum investigation. Acta Materialia. 2018;155:1–11. https://doi.org/10.1016/j.actamat.2018.05.051

10. Murdoch H et al. Tempered hardness optimization of martensitic alloy steels. Integr Mater and Manuf I. 2023;12(301–320). https://doi.org/10.1007/s40192-023-00311-9

11. Hope A. Thermo-Calc USA. Personal communication, 2022.

12. Montgomery J, Olson G. M2C carbide precipitation in AF1410. In: Krauss G, Repas PE, editors. Gilbert R. Speich Symposium Proceedings on Fundamentals of Aging and Tempering in Bainitic and Martensitic Steel Products; 1992. Iron & Steel Soc of AIME. p. 177–214.

13. Olson G, Kinkus T, Montgomery J. APFIM study of multicomponent M2C carbide precipitation in AF1410 steel. Surf Sci. 1991;246(1–3):238–245. https://doi.org/10.1016/0039-6028(91)90421-N

14. Berns H, Theisen W. Ferrous materials: steel and cast iron. Springer Science & Business Media; 2008.

15. Leitner H et al. Precipitation behaviour of a complex steel. Adv Eng Mater. 2006;8(11):1066–1077. https://doi.org/10.1002/adem.200600165

16. Szajewski BA, Crone JC, Knap J. Analytic model for the Orowan dislocation-precipitate bypass mechanism. Materialia. 2020;11:100671. https://doi.org/10.1016/j.mtla.2020.100671

17. Speich G, Dabkowski D, Porter L. Strength and toughness of Fe-10Ni alloys containing C, Cr, Mo, and Co. Metall Trans. 1973;4:303–315. https://doi.org/10.1007/BF02649630

18. Esteban-Manzanares G, Bellón B, Martínez E, Papadimitriou I, Llorca J. Strengthening of Al–Cu alloys by Guinier–Preston zones: predictions from atomistic simulations. J Mech Phys Solids. 2019;132:103675. https://doi.org/10.1016/j.jmps.2019.07.018

19. He F et al. Design of D022 superlattice with superior strengthening effect in high entropy alloys. Acta Materialia. 2019;167:275–286. https://doi.org/10.1016/j.actamat.2019.01.048

20. Szajewski B et al. Computation of metallic semicoherent interface energy for enhancing physics-based machine learning enabled alloy design. MACH Conference; 2024; Annapolis, MD.

21. Hirth JP, Lothe J. Theory of dislocations. Reprint. Krieger Publishing Company; 1992.

22. Vattré A, Abdolrahim N, Kolluri K, Demkowicz MJ. Computational design of patterned interfaces using reduced order models. Sci Rep. 2014;4(1):6231. https://doi.org/10.1038/srep06231

23. Vattré A, Demkowicz M. Determining the Burgers vectors and elastic strain energies of interface dislocation arrays using anisotropic elasticity theory. Acta Materialia. 2013;61(14):5172–5187. https://doi.org/10.1016/j.actamat.2013.05.006

24. Vattré A, Demkowicz M. Partitioning of elastic distortions at a semicoherent heterophase interface between anisotropic crystals. Acta Materialia. 2015;82:234–243.

25. Hill R. The elastic behaviour of a crystalline aggregate. Proc Phys Soc A. 1952;65(5):349. https://doi.org/10.1088/0370-1298/65/5/307

26. Razumovskiy V, Ghosh G. A first-principles study of cementite (Fe_3C) and its alloyed counterparts: structural properties, stability, and electronic structure. Comput Mater Sci. 2015;110:169–181. https://doi.org/10.1016/j.commatsci.2015.08.006

27. Ghosh G. A first-principles study of cementite (Fe_3C) and its alloyed counterparts: elastic constants, elastic anisotropies, and isotropic elastic moduli. AIP Adv. 2015;5(8). https://doi.org/10.1063/1.4928208

28. Umemoto M, Ohtsuka H. Mechanical properties of cementite. ISIJ Int. 2022;62(7):1313–1333. https://doi.org/10.2355/isijinternational.ISIJINT-2022-048

29. Tripathy H et al. High temperature thermophysical properties of spark plasma sintered tungsten carbide. Int J Refract Met Hard Mater. 2022;104:105804. https://doi.org/10.1016/j.ijrmhm.2022.105804

30. Ghosh G, Olson GB. The isotropic shear modulus of multicomponent Fe-base solid solutions. Acta Materialia. 2002;50(10):2655–2675. https://doi.org/10.1016/S1359-6454(02)00096-4

31. Darken L. Diffusion of carbon in austenite with a discontinuity in composition. Trans AIME. 1949;180:430–438.

32. Jain A et al. Commentary: the materials project: a materials genome approach to accelerating materials innovation. APL Mater. 2013;1(1). https://doi.org/10.1063/1.4812323

33. Lv ZQ et al. First-principles study on the electronic structure, magnetic properties and phase stability of alloyed cementite with Cr or Mn. J Magn Mag Mater. 2011;323(7):915–919. https://doi.org/10.1016/j.jmmm.2010.11.067

34. Nagakura S, Oketani S. Structure of transition metal carbides. Trans Iron Steel Inst Jpn. 1968;8(5):265–294. https://doi.org/10.2355/isijinternational1966.8.265

35. Xiao B et al. A comparative study of Cr7C3, Fe3C and Fe2B in cast iron both from ab initio calculations and experiments. J Phys D Appl Phys. 2009;42(11):115415. https://doi.org/10.1088/0022-3727/42/11/115415

36. Guziewski M. Multiscale study of the pearlitic microstructure in carbon steels: atomistic investigation and continuum modeling of iron and iron-carbide interfaces [PhD thesis]. Colorado State University; 2018.

37. Li Y et al. The electronic, mechanical properties and theoretical hardness of chromium carbides by first-principles calculations. J Alloys Compounds. 2011;509(17):5242–5249.

38. Krasnenko V, Brik MG. First-principles calculations of hydrostatic pressure effects on the structural, elastic and thermodynamic properties of cubic monocarbides XC (X = Ti, V, Cr, Nb, Mo, Hf). Solid State Sci. 2012;14(10):1431–1444.

39. Ivashchenko VI et al. Stability and mechanical properties of molybdenum carbides and the Ti–Mo–C solid solutions: A first-principles study. Mater Chem Phys. 2022;275:125178. https://doi.org/10.1016/j.matchemphys.2021.125178

40. Soni P, Pagare G, Sanyal SP. Structural, high pressure and elastic properties of transition metal monocarbides: A FP-LAPW study. J Phys Chem Solids. 2011;72(6):810–816. https://doi.org/10.1016/j.jpcs.2011.04.006

41. Kavitha M, Sudha Priyanga G, Rajeswarapalanichamy R, Iyakutti K. Structural stability, electronic, mechanical and superconducting properties of CrC and MoC. Mater Chem Phys. 2016;169:71–81. https://doi.org/10.1016/j.matchemphys.2015.11.031

42. Liu Y, Jiang YH, Feng J, Zhou R. Elasticity, electronic properties and hardness of MoC investigated by first principles calculations. Physica B Condens Matter. 2013;419:45–50. https://doi.org/10.1016/j.physb.2013.03.016

43. Ghosh G, Olson G. Computational thermodynamics and the kinetics of martensitic transformation. J Phase Equilibria. 2001;22:199–207. https://doi.org/10.1361/105497101770338653

44. Ohmori Y. χ-carbide formation and its transformation into cementite during the tempering of martensite. Trans Jpn Inst Metals. 1972;13(2):119–127. https://doi.org/10.2320/matertrans1960.13.119

45. Li X et al. A systematical evaluation of the crystallographic orientation relationship between MC precipitates and ferrite matrix in HSLA steels. Materials. 2022;15(11):3967. https://doi.org/10.3390/ma15113967

46. Yamasaki S. Modelling precipitation of carbides in martensitic steels [dissertation]. University of Cambridge; 2004.

47. Haghdadi N et al. Effect of ferrite-to-austenite phase transformation path on the interface crystallographic character distributions in a duplex stainless steel. Acta Materialia. 2018;145:196–209. https://doi.org/10.1016/j.actamat.2017.11.057

48. Bhadeshia HKDH. Worked examples in the geometry of crystals. International Union of Crystallography; 2001. http://www.msm.cam.ac.uk/phase-trans/2001/crystal.html

49. Zhang W-Z, Ye F, Zhang C, Qi Y, Fang H-S. Unified rationalization of the Pitsch and T–H orientation relationships between Widmanstätten cementite and austenite. Acta materialia. 2000;48(9):2209–2219. https://doi.org/10.1016/S1359-6454(00)00033-1

50. Zahiri AH, Vitral E, Ombogo J, Lotfpour M, Cao L. The role of mechanical loading in bcc-hcp phase transition: tension-compression asymmetry and twin formation. Acta Materialia. 2022;241:118377. https://doi.org/10.1016/j.actamat.2022.118377

51. Montgomery J, Olson G. Kinematics of M2C carbide precipitation. Proceedings of the 34th Sagamore Army Material Research Conference on Innovations in Ultrahigh Strength Steel Technology; 1990; Watertown, MA. US Army Materials Technology.

52. Getto E, Sun K, Was GS**.** Characterization of M2X formed during 5áMeV Fe2+ irradiation. J Nucl Mater. 2017;485:154–158. https://doi.org/10.1016/j.jnucmat.2016.12.027

53. Hu Y, Szajewski BA, Rodney D, Curtin WA. Atomistic dislocation core energies and calibration of non-singular discrete dislocation dynamics. Model Simul Mat Sci Eng. 2019;28(1):015005. https://doi.org/10.1088/1361-651X/ab5489

Appendix A. Elastic Property Equation

The bulk and shear modulus calculation of Voigt[1]:

$$B_{Voigt} = \frac{(C_{11}+C_{22}+C_{33})+2(C_{12}+C_{23}+C_{31})}{9} \quad \text{(A-1)}$$

$$G_{Voigt} = \frac{(C_{11}+C_{22}+C_{33})-(C_{12}+C_{23}+C_{31})+3(C_{44}+C_{55}+C_{66})}{15} \quad \text{(A-2)}$$

And Reuss[2]:

$$B_{Reuss} = \frac{1}{(S_{11}+S_{22}+S_{33})+2(S_{12}+S_{23}+S_{31})} \quad \text{(A-3)}$$

$$G_{Reuss} = \frac{15}{4(S_{11}+S_{22}+S_{33})-4(S_{12}+S_{23}+S_{31})+3(S_{44}+S_{55}+S_{66})} \quad \text{(A-4)}$$

Hill[3] notes that the true values should lie between the Reuss and Voigt moduli and suggest:

$$G_{RVH} = \frac{G_{Voigt}+ G_{Reuss}}{2}$$
$$B_{RVH} = \frac{B_{Voigt}+ B_{Reuss}}{2} \quad \text{(A-5)}$$

For cubic symmetry the equations reduce to:

$$G_{Voigt} = \frac{C_{11}-C_{12}+3C_{44}}{5} \quad \text{(A-6)}$$

$$G_{Reuss} = \frac{5C_{44}(C_{11}-C_{12})}{3C_{11}-3C_{12}+4C_{44}} \quad \text{(A-7)}$$

Poisson's ratio, ν, is calculated as:

$$\nu = \frac{3B_{RVH}-2G_{RVH}}{2(3B_{RVH}+G_{RVH})} \quad \text{(A-8)}$$

[1] Voigt W. Lehrbuch der kristallphysik (Leipzig: Teubner). Advances in Earth Science. 1928;1–978.

[2] Reuß A. Berechnung der fließgrenze von mischkristallen auf grund der plastizitätsbedingung für einkristalle. ZAMM-Journal of Applied Mathematics and Mechanics/Zeitschrift für Angewandte Mathematik und Mechanik. 1929;9(1):49–58.

[3] Hill R. The elastic behaviour of a crystalline aggregate. Proceedings of the Physical Society A. 1952;65(5):349. doi:10.1088/0370-1298/65/5/307

Appendix B. Precipitate Properties

The materials properties for cementite (Fe_3C) and the FCC carbide (MC) were discussed in this report's main text; the remaining 10 phases of interest are discussed in this Appendix. In the summary tables, italicized values are experimentally observed. The values in bold in each precipitate-specific table are those represented in this report's summary Tables 6 (lattice parameters) and 8 (elastic parameters), which are reproduced here in Table B-1 for each phase and used in the interfacial energy calculations.

Table B-1. Summary of lattice and elastic parameters for the 12 phases.

Phase	Avg. VM $\left[\frac{m^3}{mol}\right]\times 10^{-6}$	No. of atoms/ unit cell	Avg. V_{cell} [Å^3]	c:a (b:a) ratio	Avg. a T-C [Å]	Avg. a LIT [Å]	Shear modulus [GPa]	Poisson's ratio
				Cubic				
FCC carbide (MC)	5.75	8	76.39	1	4.24	4.17	Mo: 166.96 Cr: 167.36 V: 221.21 Ti: 181.51 Alloy: 184.26	Mo: 0.3 Cr: 0.3 V: 0.228 Ti: 0.217 Alloy: 0.26125
$M_{23}C_6$	6.20	116	1193.5	1	10.607	10.49	137.5	0.329
M_6C	7.42	112	1379.5	1	11.131	11.13	for 11.5>a>10.8: $-126.9a+1552.9$ else: 140.79	0.317
$Fe_4(C, N)$	7.10	5	47.13	1	3.612	3.75	79.64	0.36
				Hexagonal				
HCP carbide (M_2C)	6.98	3[a]	34.76[a]	1.58	2.938	2.952	149.71	0.27
MC η (hP12)[b]	8.69	33[a,b]	476.1[a,b]	2.81[b]	5.427[c]	5.068[b]	Mo: 160.81 V: 191.44 Alloy: 191.44	Mo: 0.29 V: 0.2 Alloy: 0.2
MC shp (hP2)	7.01	2[a]	23.29[a]	0.971	3.025	2.912	Mo: 232.99 W: 287.01	Mo: 0.2225 W: 0.2033
				Orthorhombic				
Cementite M_3C	5.97	16	158.7	0.880 (1.33)	5.138	5.091	Cr: 140.09 Fe: 80.41 Mn: 112.01	Cr: 0.29 Fe: 0.30 Mn: 0.335
M_3C_2	7.10	20	235.8	2.08 (0.51)	6.057	5.512	*182*	*0.26*
M_7C_3	5.89	40	391.4	2.65 (1.53)	4.586	4.49	Mn: 103.6 Fe: 107.6 Cr: 119.6 Alloy: 138.4	Mn: 0.36 Fe: 0.33 Cr: 0.33 Alloy: 0.32
				Monoclinic				
M_5C_2	5.95	28	276.6	0.44 (0.397)	11.69	11.202	Mn: 127.7 Fe: 107.9	Mn: 0.317 Fe: 0.337
KSI	7.10	44	518.4	0.6 (0.71)	11.228	10.865	71.51	0.367

[a] For primitive cell of hexagonal prism
[b] Assuming V_6C_5
[c] Average of stable MCη only
Notes: T-C = Thermo-Calc; LIT = literature; VM = molar volume

B.1 $M_{23}C_6$

The majority of stable $M_{23}C_6$ phases are $Cr_{23}C_6$ with some solubility of other elements (Figure B-1); the Cr-based carbides have larger lattice parameters than the Fe-based, which matches literature results (Table B-2). The metastable $M_{23}C_6$ phases include more mixed Fe-based carbides, particularly $(Fe, Mn)_{23}C_6$, which also have a smaller lattice parameter than the Cr-based, as expected. No trend was observed for shear modulus or Poisson's ratio as a function of lattice parameter or primary element (Figure B-2); furthermore, since most of the carbides are multicomponent, we use the average value of μ and ν.

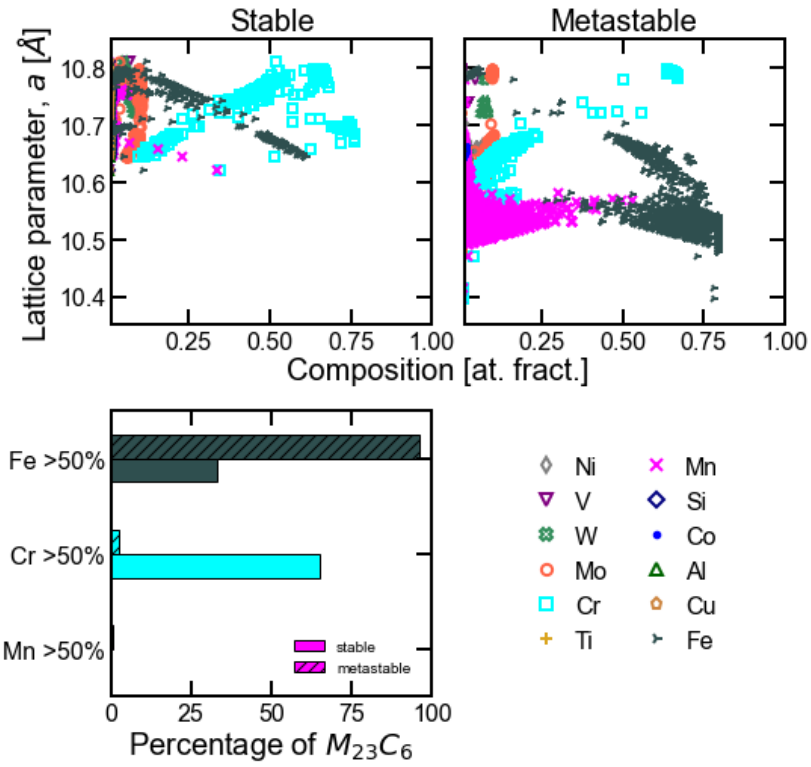

Figure B-1. Compositions of stable and metastable $M_{23}C_6$ phases predicted from Thermo-Calc and corresponding lattice parameters calculated using Table B-1.

Table B-2. Elastic and lattice parameters from literature for $M_{23}C_6$.

Phase	Ref.	G_{Hill} [GPa]	ν	$a=b=c$ [Å]
$Cr_{23}C_6$	[1]	. . .	. . .	*10.659*
	[2]	146.78	0.31	10.55
	[3]	132.19	0.33	10.39
	[4]	134.16	0.32	10.537
	[5]	145.45	0.30	10.554
$(Cr, W)_{23}C_6$	[1]	. . .	. . .	*10.66*
$Fe_{23}C_6$	[3]	126.98	0.35	10.16
$Fe_{23}C_6$	[4]	118.43	0.36	10.453
$Fe_{21}Cr_2C_6$	[3]	148.59	0.33	10.17
$(Fe, Cr)_{23}C_6$	[1]	. . .	. . .	*10.59*
$Fe_{21}Mo_2C_6$	[3]	156.01	0.32	10.26
$(Fe, Cr, Mo, W)_{23}C_6$	[1]	. . .	. . .	*10.67*
$(Fe, Cr, Mo, V, W)_{23}C_6$	[1]	. . .	. . .	*10.58*
$Fe_{21}W_2C_6$	[1]	. . .	. . .	*10.56*
$Mn_{23}C_6$	[1]	. . .	. . .	*10.585*
	[6]	. . .	. . .	*10.595*
	[3]	129.51	0.34	10.39
	[3]	136.82	0.33	10.43
		137.5	**0.329**	**10.49**

Note: italics indicate experimentally measured lattice parameters

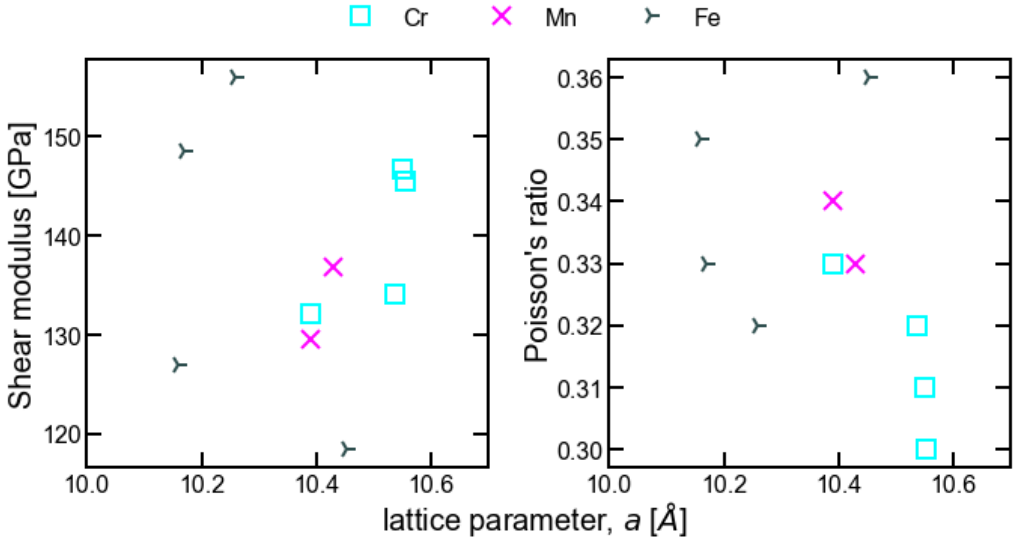

Figure B-2. Elastic parameters for $M_{23}C_6$ as a function of lattice parameter and primary element.

B.2 $_6$C

The structure of the M_6C phase as dictated by Thermo-Calc requires either W or Mo; as such, the M_6C carbides are generally $(Fe, Mo)_6C$ or $(Fe, W)_6C$. From the Thermo-Calc results, Mo is found to increase the lattice parameter while W decreases the lattice parameter, which is generally borne out by the observations in Table B-3. The metastable carbides include a large proportion of $Fe_2(Mo, Si)_4C$,

see Figure B-3. We were unable to find any experimental evidence for this carbide, only a similar $(Ni, Si)_3Mo_3C$.[7] Both Mo and Si are slow diffusers and as such M_6C phases like $Fe_2(Mo,Si)_4C$ would not be kinetically favored to form except in regions of high segregation (e.g., interdendritic regions); this makes them unlikely to be experimentally observed.

Table B-3. Elastic and lattice parameters from literature for M_6C.

Phase	Ref.	G_{Hill} [GPa]	v	$a=b=c$ [Å]
	[1]	. . .	. . .	*11.06*
	[8]	. . .	. . .	*11.087*
Fe_3W_3C	[8]	160.92	0.31	11.026
	[9]	182.22	0.31	10.84
	[10]	170.04	0.31	11.02
Fe_4W_2C	[1]	. . .	. . .	*11.10*
$(Fe, W, V)_6C$	[1]	. . .	. . .	*11.06*
Fe_2VW_3C	[8]	137.22	0.31	11.1829
FeV_2W_3C	[8]	121.63	0.34	11.2715
Fe_2CrW_3C	[8]	144.97	0.32	11.0761
Fe_2MnW_3C	[8]	163.07	0.31	11.0385
Fe_2CoW_3C	[8]	155.30	0.30	11.0185
$FeCr_2W_3C$	[8]	133.27	0.33	11.1538
$FeCr_2W_3C$	[1]	. . .	. . .	*11.07*
$(Fe, Cr)_4W_2C$	[1]	. . .	. . .	*11.05*
$FeMn_2W_3C$	[8]	145.63	0.30	11.0613
$FeCo_2W_3C$	[8]	140.30	0.30	11.0745
Fe_2NiW_3C	[8]	147.16	0.29	11.0336
$FeNi_2W_3C$	[8]	133.99	0.29	11.0857
Fe_2TiW_3C [x]	[8]	126.27	0.32	11.2991
$FeTi_2W_3C$ [x]	[8]	95.77	0.36	11.4456
	[1]	. . .	. . .	*11.14*
Fe_3Mo_3C	[11]	137.86	0.31	11.025
	[11]	. . .	. . .	*11.077*
Fe_2Mo_4C	[11]	125.58	0.32	11.266
	[1]	. . .	. . .	*11.26*
$FeMo_5C$ [x]	[11]	98.35	0.36	11.493
$(Fe, Mo, Cr)_6C$	[1]	. . .	. . .	11.08
$(Mo, Fe)_6C$	[1]	. . .	. . .	12.0
$(Fe, Mo, V)_6C$	[1]	. . .	. . .	*11.09*
$(Fe, Mo, W)_6C$	[1]	. . .	. . .	*11.09*
Co_2Mo_4C	[1]	. . .	. . .	*11.25*
	[8]	143.21	0.31	11.0398
Co_3W_3C	[8]	. . .	. . .	*11.112*
	[9]	158.10	0.33	10.88
Co_2W_4C	[1]	. . .	. . .	*11.21*
	[8]	133.21	0.31	11.0651
	[1]	. . .	. . .	*11.17*
Ni_3W_3C	[9]	143.41	0.33	10.9
M_6C		**Equation B-1**	**0.317**	**11.13**

Note: italics indicate experimentally measured lattice parameters

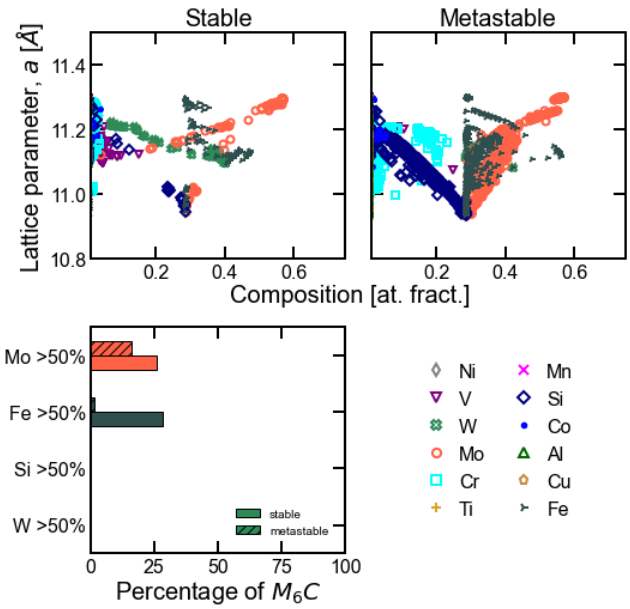

Figure B-3. Compositions of stable and metastable M_6C phases predicted from Thermo-Calc and corresponding lattice parameters calculated using Table B-1.

All M_6C carbides that appear in this dataset include some fraction of Fe, but we include a few non-Fe containing M_6C carbides in Table B-3 for reference. Overall, both the stable and metastable lattice parameters have very good agreement between the predictions from Thermo-Calc and the observations in Table B-3.

We plot the shear modulus and Poisson's ratio variation with respect to lattice parameter and primary element for the M_6C carbides from Table B-3 in Figure B-4. In other phases, there can be obvious correlations between the elastic parameters and the majority element in the carbide; here, due to the heavily mixed microstructures, a relationship is more evident between the lattice parameter and the shear modulus. A linear relationship is fit to the Fe-containing carbides (i.e., not the Co_3W_3C or Ni_3W_3C, which are still plotted for reference but not observed in this dataset):

$$\mu_{M_6C}\,[GPa] = -126.9\,a[\text{Å}] + 1552.9 \qquad \text{(B-1)}$$

We use this equation between the lattice parameter bounds of 10.8 and 11.5; this dataset does not have any lattice parameters outside these bounds, but we include them for future reference. If the calculated lattice parameter is outside these bounds, then the shear modulus average of 140.79 GPa is assumed.

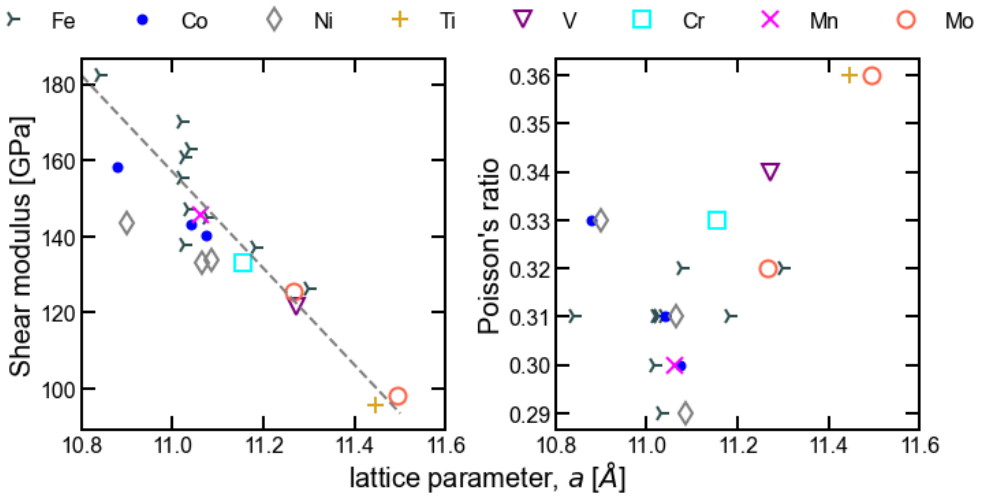

Figure B-4. Elastic parameters for M_6C as a function of lattice parameter and primary element. A linear relationship between lattice parameter and shear modulus is presented.

B.3 $Fe_4(C,N)$

The $Fe_4(C,N)$ phase is never observed as a stable equilibrium phase across the compositions and temperatures of this dataset, only in a metastable state (Figure B-5). The lattice parameter does not vary considerably with composition. From Table B-4, calculations of the lattice parameter are very consistent despite compositional variation, whether all N or all C and whether all Fe or all Cr. Cr_4N has not been experimentally observed, but we include it here as a possible bound to the variability in materials data. Only 13 of the 1749 observations of this phase in this dataset are actually Fe_4N, most are Fe_4C. It is therefore unsurprising that this phase is never considered stable, as Fe_4C is unstable compared to other Fe-C carbides.[12] However, the theoretical values of shear modulus and Poisson's ratio for Fe_4C are used for the elastic interfacial energy calculations since most of the predicted phases from Thermo-Calc fall into this composition space.

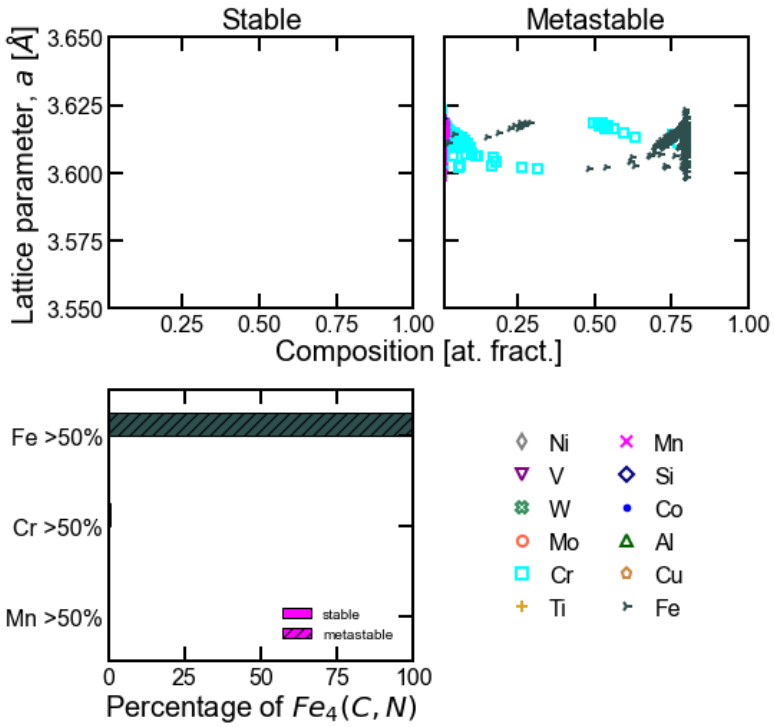

Figure B-5. Compositions of stable and metastable $Fe_4(C,N)$ phases predicted from Thermo-Calc and corresponding lattice parameters calculated using Table B-1.

Table B-4. Elastic and lattice parameters from literature for $Fe_4(C,N)$ phase.

Phase	Ref.	G_{Hill} [GPa]	ν	$a=b=c$ [Å]
Fe_4N	[13]	63.48	0.36	3.77
Fe_4N	[14]	59.83	0.38	3.79
Fe_4N	[15]	63.66	0.37	3.78
Cr_4N	[16]	97.77	0.36	3.77
Fe_4C	[15]	**79.64**	**0.36**	**3.75**

B.4 M_2C

Most of the predicted M_2C phases are Mo-based with some Cr-based (Figure B-6). The decrease observed in the predicted lattice parameter when substituting atoms for Mo is consistent with literature.[17] The dashed lines represent the average literature lattice parameter, *a*, from Table B-5 for Mo_2C, V_2C, and Cr_2C, respectively. There is excellent agreement between the predicted and literature lattice parameters.

There are no trends in the elastic parameters as a function of primary element or lattice parameter (Figure B-7). An average shear modulus and Poisson ratio are therefore chosen for the phase.

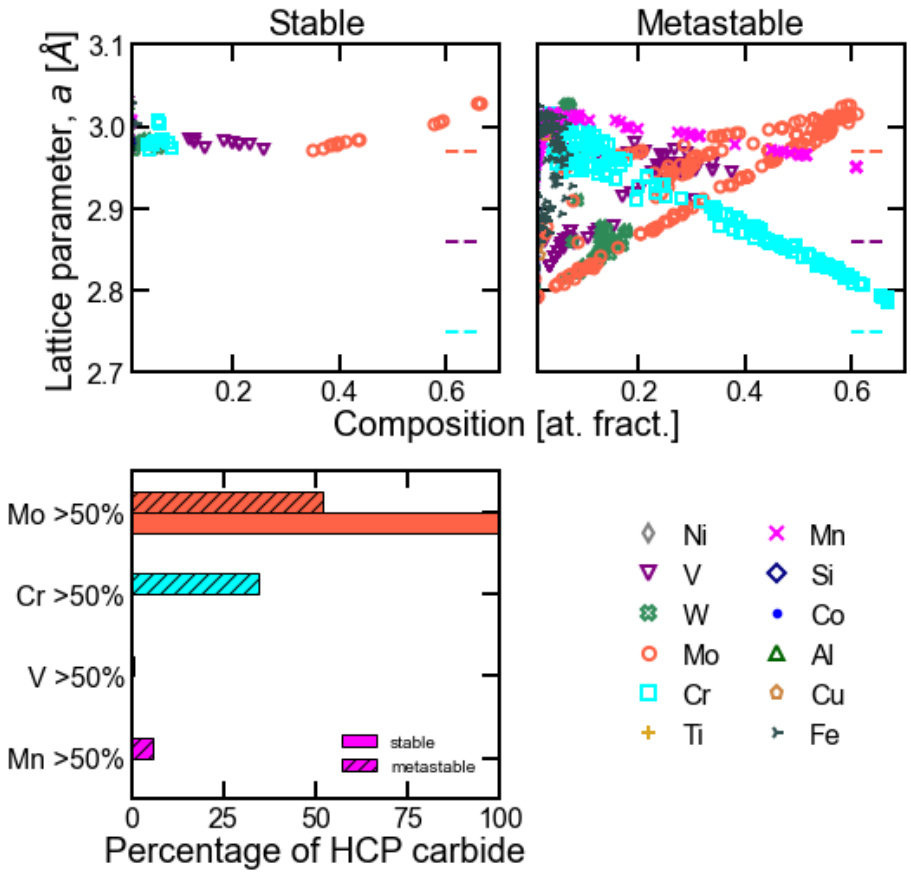

Figure B-6. Compositions of stable and metastable M_2C phases predicted from Thermo-Calc and corresponding lattice parameters calculated using Table B-1.

Table B-5 Elastic and lattice parameters from literature for M_2C.

Phase	Ref.	G_{Hill} [GPa]	ν	a [Å]	c [Å]	c:a
	[1]	. . .	. . .	*2.997–3.012*	*4.727–4.736*	*1.57*
	[18]	. . .	. . .	2.98	4.73	1.59
	[19]	. . .	. . .	3.0	4.73	1.58
	[20]	. . .	. . .	2.88	4.52	1.57
	[23]	. . .	. . .	3.054	4.652	1.52
Mo_2C	[17]	146.85	0.29	3.036	4.705	1.55
	[23]	155.17	0.25	3.054	4.653	1.52
	[24]	200.38	0.27	2.926	5.373	1.84
	[21]	143.4	0.28	3.07	4.66	1.52
	[3]	157.74	0.27	3.030	4.7	1.55
	[22]	133.04	0.25	3.003	4.743	1.58
Mo_7CrC_4	[22]	138.01	0.26	. . .	. . .	. . .
Mo_7WC_4	[22]	174.39	0.22	. . .	. . .	. . .
$Mo_6W_2C_4$	[22]	123.93	0.25	. . .	. . .	. . .
Mo_6WCrC_4	[22]	137.37	0.29	. . .	. . .	. . .
MoCrC	[23]	. . .	. . .	2.946	4.459	1.51
$(Mo,Cr)_2C$	[17]	153.68	0.28	3.002	4.652	1.55
$(Mo,V)_2C$	[17]	161.53	0.28	3.013	4.670	1.55
$(Mo,Fe)_2C$	[17]	144.15	0.29	2.994	4.640	1.55
$(Mo,W)_2C$	[17]	159.28	0.28	3.036	4.705	1.55
Cr_2C	[25]	. . .	. . .	2.71	4.52	1.67
$(Cr,Fe)_2C$	[26]	. . .	. . .	2.79	4.4	1.58
Cr_2C	[27]	129.03	0.25	2.833	4.259	1.50
	[28]	. . .	. . .	2.8	4.5	1.61
V_2C	[29]	. . .	. . .	2.9	4.57	1.58
	[1]	. . .	. . .	*2.884–2.904*	*4.568–4.588*	*1.58*
	[30]	137.41	0.31	2.884	4.797	1.66
W_2C	[1]	. . .	. . .	3.001	4.736	1.58
M_2C		**149.71**	**0.27**	**2.952**		**1.58**

Note: italics indicate experimentally measured lattice parameters

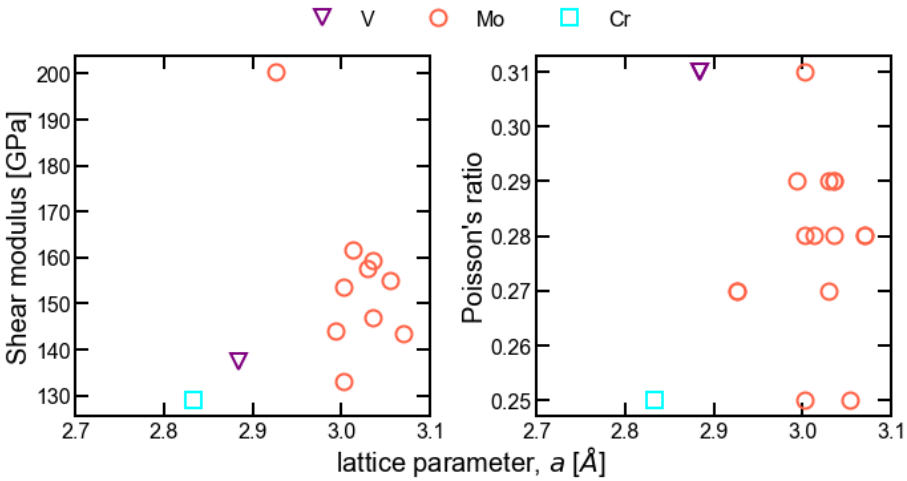

Figure B-7. Elastic parameters as a function of lattice parameter and composition for M_2C.

B.5 MC_{η} and MC_{SHP}

Thermo-Calc differentiates between two hexagonal MC phases with the subscript "SHP" (simple hexagonal phase) for $(Mo, W)_1(C, N)_1$ with structure hP2 ($P\bar{6}m2$) and subscript "η" for $(Mo, Ti, V, W)_1(C, Va)$ with structure hP12 ($P6_3/mmc$) where Va is vacancies.

The MC_{SHP} phases are straightforward, with the stable and metastable phases both consisting of either MoC or a mixture of W and Mo in (W, Mo)C (Figure B-8). There is not much variability in lattice parameter with alloy content, but the elastic parameters between a Mo- and W-based carbide are different, with W-based having a higher shear modulus (Table B-6). Consequently, average elastic properties are determined for either the Mo- or W-based carbides for use in the interfacial energy calculations.

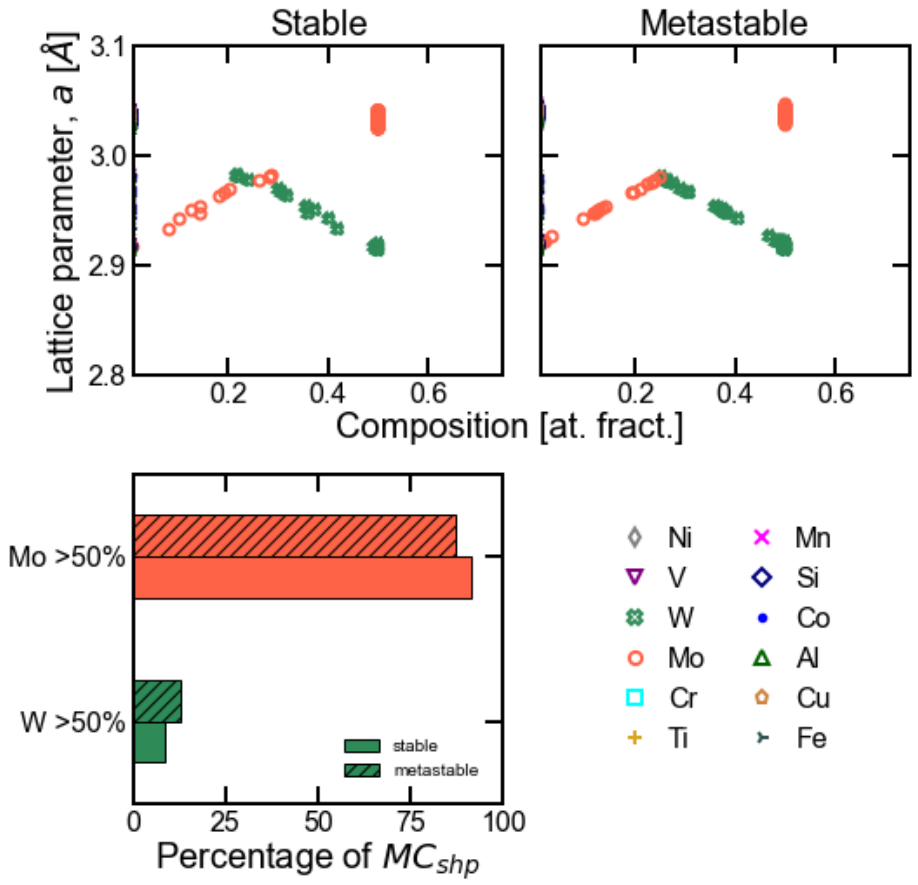

Figure B-8. Compositions of stable and metastable MC_{SHP} phases predicted from Thermo-Calc and corresponding lattice parameters calculated using Table B-1.

Table B-6. Elastic and lattice parameters from literature for MC_{SHP}.

	Ref.	G_{Hill} [GPa]	ν	a = b [Å]	c [Å]	c:a
WC	[1]	. . .	. . .	*2.906*	*2.837*	*0.976*
	[31]	296.05	0.19	2.926	2.849	0.974
	[32]	278.82	0.21	2.92	2.84	0.973
	[33]	286.16	0.21	2.906	2.825	0.972
W-based		**287.01**	**0.2033**			
MoC	[1]	. . .	. . .	*2.898*	*2.809*	*0.969*
	[34]	213.95	0.23	2.91	2.83	0.973
	[21]	255.1	0.21	2.926	2.840	0.971
	[21]	239	0.22	2.898	2.809	0.969
	[21]	223.9	0.23	2.926	2.834	0.969
	[21]	. . .	. . .	2.901	2.786	0.960
Mo-based		**232.99**	**0.2225**			
				2.912		**0.971**

Note: italics indicate experimentally measured lattice parameters

The Thermo-Calc prototype for MC_η is η-MoC_{1-x}, which is experimentally observed at high temperatures (>1658 °C) and in C ranges around approximately 37–40 at%. Only one report of experimental observation below 1658 °C could be found[35] despite thermodynamic assessments consistently predicting lower temperature stability.[36] The experimental lattice parameter measurement for η-MoC in Table B-7 was formed at both high temperature (1750 °C) and pressure. The frequent prediction by Thermo-Calc of a low temperature η-MoC is somewhat anomalous; further, the large composition range is inconsistent with the purported carbide phase structure (Figure B-9). There are also some metastable hexagonal W_2C phases present that should be in the HCP carbide group (M_2C), but not here. We therefore do not include the MoC lattice ratios when considering the average ratio for c:a for the MC_η phase.

V_6C_5 is another experimentally observed hexagonal (sometimes labeled trigonal) phase that more correctly aligns with the reported prototype stoichiometry; the stable MC_η phases are also volume (V)-based. Therefore, we use the lattice parameters of V_6C_5 for the ratio in Table B-1 instead of MoC_{1-x}. This results in the least congruence between the average experimental lattice parameter and average Thermo-Calc lattice parameter of all the phases explored herein. We also use the #/atoms unit cell and elastic parameters for V_6C_5.

The elastic constants for the MC_η phase are then tabulated as either the Mo- or V-based carbides. Given the anomalous behavior of the Mo-based phase, alloy carbides are assumed to have the same properties of the V-based phase.

Table B-7. Elastic and lattice parameters from literature for MCη.

Phase	Ref.	G_{Hill} [GPa]	ν	a = b [Å]	c [Å]	c:a
MoC_{1-x}	[1]	. . .	. . .	*3.013*	*14.64*	4.86
	[3]	**160.81**	**0.29**	3.03	15.6	5.15
	[21]	. . .	. . .	3.082	15.361	4.98
V_6C_5	[37]	181.58	0.19	5.101	14.354	2.81
	[38]	180.66	0.2	5.099	14.345	2.81
	[30]	212.09	0.2	5.005	14.099	2.82
V-based		**191.44**	**0.2**	**5.068**		**2.81**

Note: italics indicate experimentally measured lattice parameters

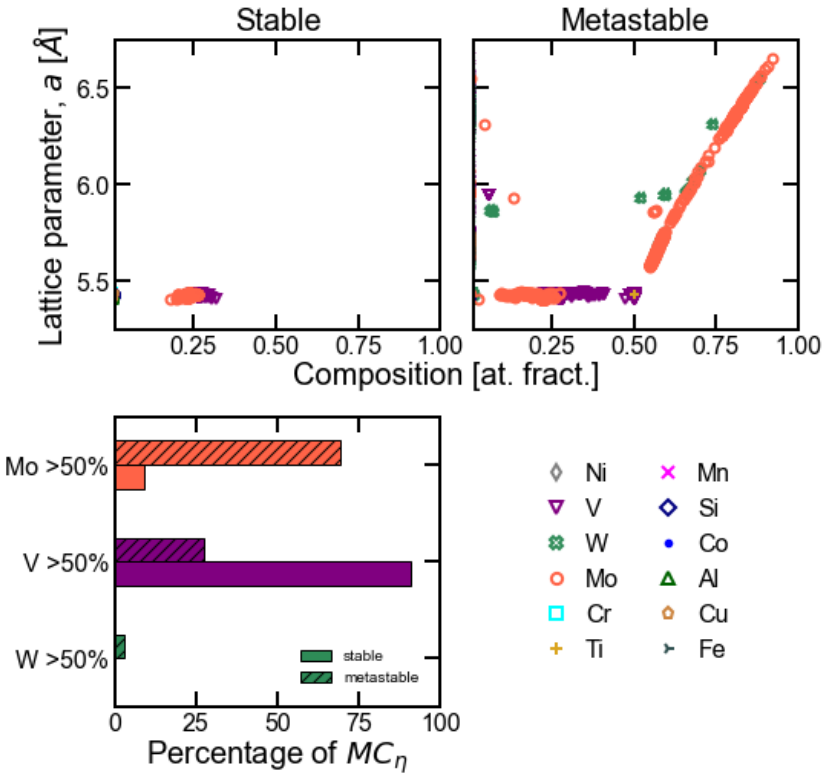

Figure B-9. Compositions of stable and metastable MC_η phases predicted from Thermo-Calc and corresponding lattice parameters calculated using Table 6.

B.6 M_7C_3

There is a mix of predicted M7C3 phases, including mostly Cr,Mo-based stable phases and many metastable mixed carbides (Figure B-10). There is excellent agreement between the predicted and literature lattice parameters.

Interestingly, the mixed carbides seem to have much larger shear moduli than the single-component carbides (Table B-8). We therefore separate out the elastic parameters of the mixed carbides when calculating averages. There is no particular trend between lattice parameter and elastic properties (Figure B-11) as there was in the M_6C phase, which also had significantly mixed compositions.

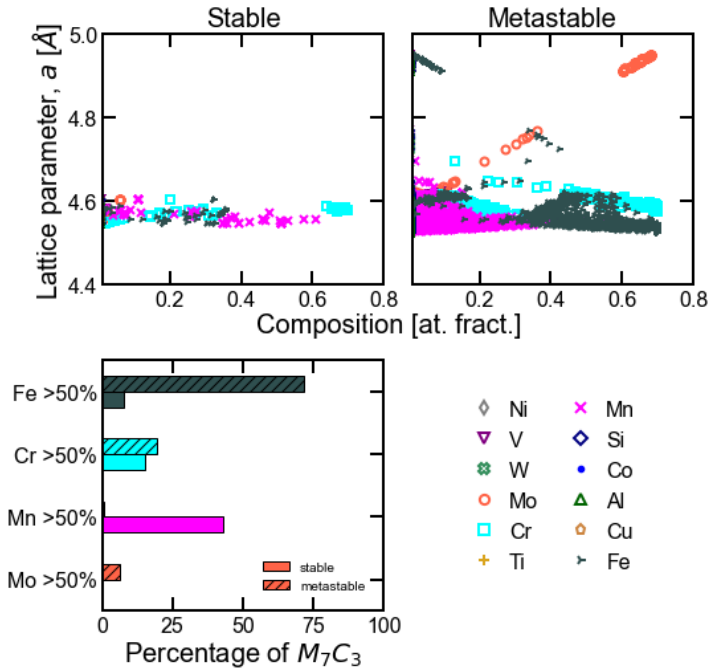

Figure B-10. Compositions of stable and metastable M_7C_3 phases predicted from Thermo-Calc and corresponding lattice parameters calculated using Table B-1.

Table B-8. Elastic and lattice parameters from literature for M_7C_3.

	Ref.	G_{Hill} [GPa]	ν	a [Å]	b [Å]	c [Å]	c:a	b:a
Mn_7C_3	[1]	. . .	. . .	*4.546*	*6.959*	*11.979*	*2.635*	*1.531*
	[6]	. . .	. . .	*4.543*	*6.954*	*11.973*	*2.635*	*1.531*
	[39]	103.6	0.36	4.475	6.868	11.903	2.660	1.535
Mn-based		**103.6**	**0.36**					
Fe_7C_3	[40]	107.97	0.30	4.48	6.55	11.8	2.634	1.462
	[39]	117.9	0.36	4.33	6.67	11.4	2.633	1.540
	[41]	99.6	0.316	4.515	6.862	11.724	2.597	1.520
	[1]	. . .	. . .	*4.54*	*6.879*	*11.942*	*2.630*	*1.515*
	[42]	104.98	0.34	. . .	. . .	. . .	. . .	. . .
Fe-based		**107.6**	**0.33**					
Cr_7C_3	[2]	133.10	0.33	4.45	6.84	11.97	2.690	1.537
	[43]	113	0.338	. . .	. . .	. . .	. . .	. . .
	[41]	90.11	0.368	4.488	6.934	12.017	2.678	1.545
	[5]	118	0.33	4.511	6.903	12.08	2.678	1.530
	[44]	143.85	0.30	4.526	7.01	12.142	2.683	1.549
Cr-based		**119.6**	**0.33**					
$Fe_3Cr_4C_3$	[41]	106.3	0.324	4.526	6.851	11.808	2.609	1.514
$Fe_{16}Cr_{12}C_{12}$	[43]	119.6	0.338	. . .	. . .	. . .	. . .	. . .
$Fe_{12}Cr_{12}W_4C_{12}$	[43]	133.6	0.333	. . .	. . .	. . .	. . .	. . .
$Fe_{12}Cr_{12}Mo_4C_{12}$	[43]	127.6	0.338	. . .	. . .	. . .	. . .	. . .
$(Fe, Cr)_7C_3$	[44]	152.40	0.3	. . .	. . .	. . .	. . .	. . .
$(Fe, Cr, Mo)_7C_3$	[44]	164.05	0.3	. . .	. . .	. . .	. . .	. . .
$(Fe, Cr, W)_7C_3$	[44]	165.50	0.30	. . .	. . .	. . .	. . .	. . .
Alloy		**138.4**	**0.32**					
				4.49			**2.65**	**1.53**

Note: italics indicate experimentally measured lattice parameters

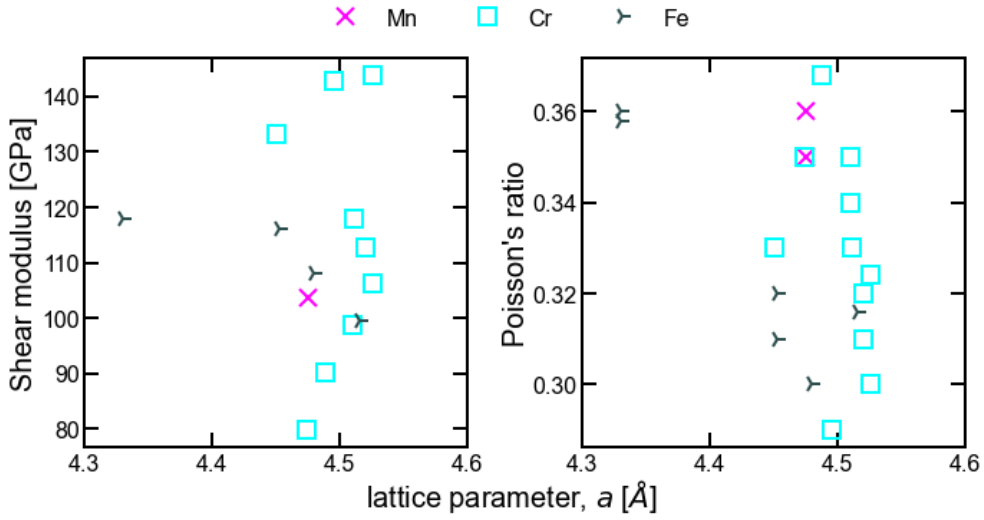

Figure B-11. Elastic parameters as a function of lattice parameter and composition for M_7C_3.

B.7 M_3C_2

The predicted stable M_3C_2 phases are all Cr_3C_2; metastable phases are also mostly Cr-based with a few V- and Mo- based carbides (Figure B-12). Only information about Cr_3C_2 was found in the literature (Table B-9). He et al.[45] has experimentally measured the elastic parameters, so we use those values instead of taking an average of modeling values as we have done for other phases.

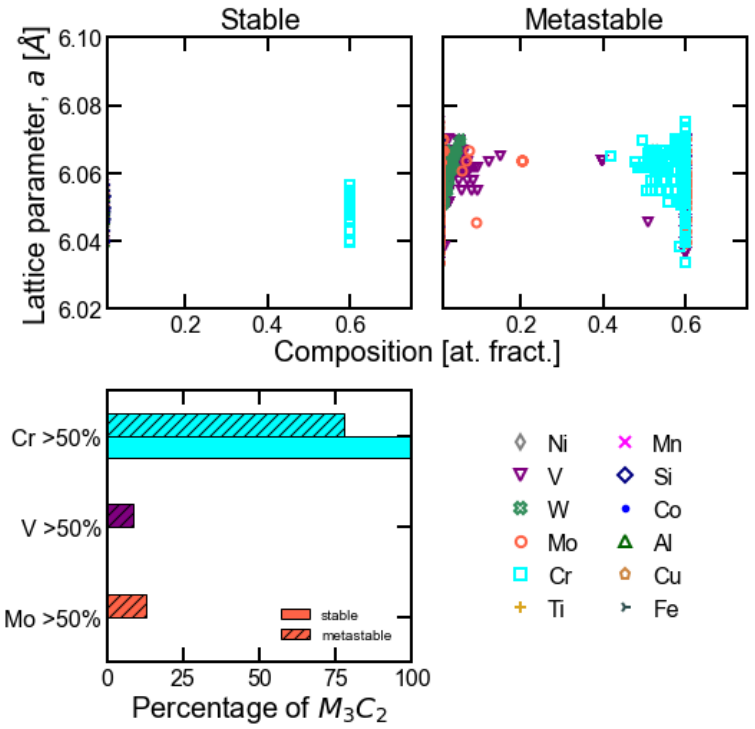

Figure B-12. Compositions of stable and metastable M_3C_2 phases predicted from Thermo-Calc and corresponding lattice parameters calculated using Table B-1.

Table B-9. Elastic and lattice parameters from literature for M_3C_2.

Phase	Ref.	G_{Hill} [GPa]	ν	a [Å]	b [Å]	c [Å]	c:a	b:a
Cr_3C_2	[1]	. . .	. . .	*5.53*	*2.827*	*11.48*	*2.08*	*0.51*
	[2]	166.10	0.28	5.48	2.79	11.47	2.09	0.51
	[5]	146.80	0.28	5.485	2.789	11.474	2.09	0.51
	[5]	162.00	0.29	5.554	2.833	11.494	2.07	0.51
	[45]	163.2	0.28	. . .	. . .	. . .	. . .	. . .
	[45]	*182*	*0.26*	. . .	. . .	. . .	. . .	. . .
		182	***0.26***	**5.512**			**2.08**	**0.51**

Note: italics indicate experimentally measured parameters

B.8 $_5C_2$ and KSI-carbide

The M_5C_2 (Hägg carbide) is most often observed experimentally as a precursor to the cementite phase,[46,47] so it is unsurprising that it is only predicted to be a metastable phase (Figure B-13). These metastable carbides are majority Fe-based with some Mn-based. Elastic constants between Mn_5C_2 and Fe_5C_2 are somewhat different (Table B-10), therefore they will be assigned based on the majority element. The sole literature value is used for the Mn_5C_2, while an average of literature values is used for Fe_5C_2. Increasing the Mn content increases the lattice parameter, which is consistent with experimental results. The calculated lattice parameters for Fe_5C_2 from various density functional theory (DFT) approaches are somewhat disparate (especially Guzierwski[40]) from the experimentally measured lattice parameters (italics in Table B-10); therefore the average lattice ratios a:c and a:b are calculated only from the experimental measurements.

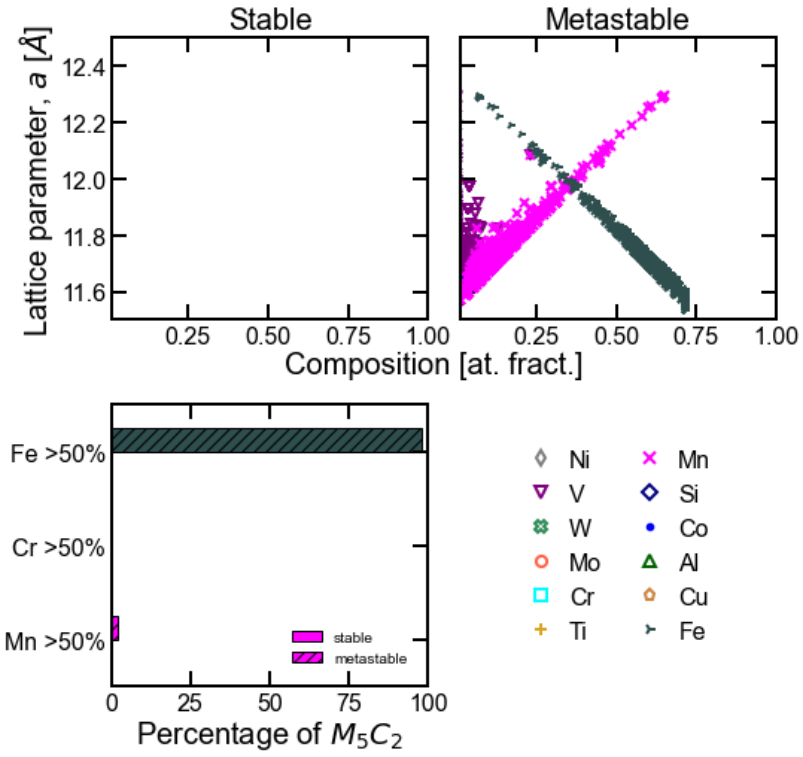

Figure B-13. Compositions of stable and metastable M_5C_2 phases predicted from Thermo-Calc and corresponding lattice parameters calculated using Table B-1.

Table B-10. Elastic and lattice parameters from literature for M_5C_2.

	Ref.	G_{Hill} [GPa]	ν	a [Å]	b [Å]	c [Å]	c:a	b:a
Mn_5C_2	[1]	. . .	. . .	*11.66*	*4.573*	*5.08*	*0.44*	*0.39*
	[6]	. . .	. . .	*11.67*	*4.586*	*5.097*	*0.44*	*0.39*
	[48]	127.7	0.317	11.717	4.51	4.978	0.42	0.38
Mn-based		**127.7**	**0.317**					
Fe_5C_2	[1]	. . .	. . .	*11.56*	*4.573*	*5.058*	*0.44*	*0.40*
	[49]	89.16	0.33	11.575	4.5102	4.993	0.43	0.39
	[40]	102.00	0.33	10	4.53	4.95	0.50	0.45
	[40]	123.01	0.32	10.2	4.47	4.85	0.48	0.44
	[39]	128.8	0.34	11.19	4.36	4.82	0.43	0.39
	[50]	96.53	0.368	11.25	4.538	5.021	0.45	0.40
Fe-based		**107.9**	**0.337**					
				11.202			***0.44[a]***	***0.40[a]***

[a] Average calculated from experimental measurements only
Note: italics indicate experimentally measured lattice parameters

The KSI carbide is often called a Mo-cementite (e.g., Mo_3C)[51] and is close in composition. As no elastic constants could be found for the KSI carbide in the stoichiometry used in the Thermo-Calc database, those of the $(Fe,Mo)_3C$ (Mo-cementite) shown in Table B-11 are used. The KSI carbide is mostly predicted to be metastable with a small variation in lattice parameter with Cr/Mo content (Figure B-14).

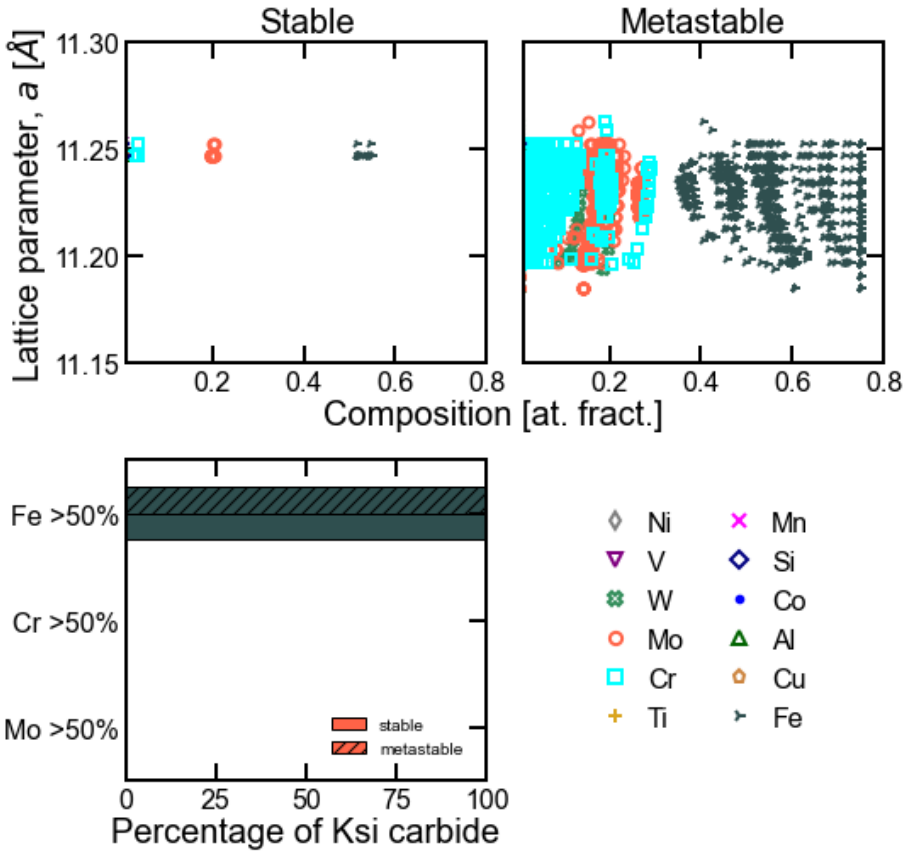

Figure B-14. Compositions of stable and metastable KSI-carbide phases predicted from Thermo-Calc and corresponding lattice parameters calculated using Table B-1.

Table B-11. Elastic and lattice parameters from literature for the KSI carbide.

Phase	Ref.	G_{Hill} [GPa]	ν	a [Å]	b [Å]	c [Å]	c:a	b:a
$Mo_{12}Fe_{22}C_{10}$	[51]	. . .	. . .	*10.865*	*7.767*	*6.559*	*0.60*	*0.71*
~Mo_3C	[52]	71.63	0.377	. . .	. . .	. . .	. . .	. . .
$Mo_1Fe_{11}C_4$	[53]	71.39	0.357	. . .	. . .	. . .	. . .	. . .
		71.51	**0.367**	**10.865**			**0.60**	**0.71**

Note: italics indicate experimentally measured lattice parameters

B.9 References

1. Nagakura S, Oketani S. Structure of transition metal carbides. Trans Iron Steel Inst Jpn. 1968;8(5):265–294. https://doi.org/10.2355/isijinternational1966.8.265

2. Sun L et al. First principles investigation of binary chromium carbides Cr7C3, Cr3C2 and Cr23C6: electronic structures, mechanical properties and thermodynamic properties under pressure. Materials. 2022;15(2):558. https://doi.org/10.3390/ma15020558

3. Liu Y, Yehua J, Jiandong X, Rong Z, Jing F. Mechanical properties and electronic structures of M23C6 (M= Fe, Cr, Mn)-type multicomponent carbides. J Alloys Comps. 2015;648:874–880. https://doi.org/10.1016/j.jallcom.2015.07.048

4. Wu Y et al. Insights to electronic structures, elastic properties, fracture toughness, and thermal properties of M23C6 carbides. Int J Refract Metal Hard Mater. 2022;109:105985. https://doi.org/10.1016/j.ijrmhm.2022.105985

5. Li Y et al. The electronic, mechanical properties and theoretical hardness of chromium carbides by first-principles calculations. J Alloys Compounds. 2011;509(17):5242–5249. https://doi.org/10.1016/j.jallcom.2011.02.009

6. Karen P et al. On phase relations, structural and magnetic properties of the stable manganese carbides Mn23C6, Mn5C2 and Mn7C3. Acta Chemica Scandinavica. 1991;45:549–557. https://doi.org/10.3891/acta.chem.scand.45-0549

7. Jiang L et al. The critical role of Si doping in enhancing the stability of M6C carbides. J Alloy Compd. 2017;728:917–926. https://doi.org/10.1016/j.jallcom.2017.09.042

8. Suetin DV, Medvedeva NI. First-principles study of structure, magnetic properties, and stability of η-carbides (M,Fe)3W3C (M = Ti, V, Cr, Mn, Co, and Ni). Phys Status Solidi B. 2019;256(12):1900108. https://doi.org/10.1002/pssb.201900108

9. Li Y et al. First-principles study on the stability and mechanical property of eta M3W3C (M=Fe, Co, Ni) compounds. Phys B Condens Matter. 2010;405(3):1011–1017. https://doi.org/10.1016/j.physb.2009.10.045

10. Li Z et al. Formation mechanism and stability of the phase in the interface of tungsten carbide particles reinforced iron matrix composites: First principles

calculations and experiments. J Mater Res. 2016;31(16):2376–2383. https://doi.org/10.1557/jmr.2016.268

11. Lv ZQ, Wang B, Sun SH, Fu WT. Effect of atomic sites on electronic and mechanical properties of (Fe,Mo)6C carbides. J Alloy Compd. 2015;649:1089–1093. https://doi.org/10.1016/j.jallcom.2015.06.249

12. Leineweber A, Hickel T, Azimi-Manavi B, Maisel SB. Crystal structures of Fe4C vs. Fe4N analysed by DFT calculations: FCC-based interstitial superstructures explored. Acta Materialia. 2017;140:433–442. https://doi.org/10.1016/j.actamat.2017.08.059

13. Cheng C-H et al. Magnetic and mechanical properties of deformed iron nitride-Fe 4 N. J Appl Math. 2015. https://doi.org/10.1155/2015/238730

14. Takahashi T, Burghaus J, Music D, Dronskowski R, Schneider JM. Elastic properties of γ′-Fe4N probed by nanoindentation and ab initio calculation. Acta Materialia. 2012;60(5):2054–2060. https://doi.org/10.1016/j.actamat.2011.12.051

15. Lv ZQ et al. Electronic, magnetic and elastic properties of γ-Fe4X (X=B/C/N) from density functional theory calculations. J Magn Magn Mater. 2013;333:39–45. https://doi.org/10.1016/j.jmmm.2012.12.044

16. Adhikari V et al. First-principles study of mechanical and magnetic properties of transition metal (M) nitrides in the cubic M4N structure. J Phys Chem Solids. 2018;120:197–206. https://doi.org/10.1016/j.jpcs.2018.04.043

17. Sun C et al. Optimization of thermal stability and mechanical properties of Mo2C carbides via multi-element doping: experimental and theoretical calculations. J Mater Sci. 2022;57(34):16352–16366. https://doi.org/10.1007/s10853-022-07693-9

18. Lee HM, Sohn H, Yoo CH. Isothermal M2C carbide growth in ultrahigh strength high Co-Ni steels. Scripta Materialia. 1997;37(12):1931–1937. https://doi.org/10.1016/S1359-6462(97)00385-0

19. Ayer R, Machmeier P. Transmission electron microscopy examination of hardening and toughening phenomena in Aermet 100. Metall Trans A. 1993;24:1943–1955. https://doi.org/10.1007/BF02666329

20. Montgomery J, Olson G. M2C carbide precipitation in AF1410. In: Krauss G, Repas PE, editors. Gilbert R. Speich Symposium Proceedings on Fundamentals of Aging and Tempering in Bainitic and Martensitic Steel Products; 1992. Iron & Steel Soc of AIME. p. 177–214.

21. Ivashchenko VI et al. Stability and mechanical properties of molybdenum carbides and the Ti–Mo–C solid solutions: a first-principles study. Mater Chem Phys. 2022;275:125178. https://doi.org/10.1016/j.matchemphys.2021.125178

22. Wu D, Fu W-T, Li Y, Wang C-X, Tang J-L. Phase stability, elastic, thermo-physical and electronic properties of hexa-(Mo,Cr,W)2C from first-principles calculations. J Iron Steel Res Int. 2016;23(10):1096–1103. https://doi.org/10.1016/S1006-706X(16)30162-5

23. Liu H, Zhu J, Lai Z, Zhao R, He D. A first-principles study on structural and electronic properties of Mo2C. Scripta Materialia. 2009;60(11):949–952. https://doi.org/10.1016/j.scriptamat.2009.02.010

24. Naher MI, Naqib SH. Possible applications of Mo2C in the orthorhombic and hexagonal phases explored via ab-initio investigations of elastic, bonding, optoelectronic and thermophysical properties. Results Phys. 2022;37:105505. https://doi.org/10.1016/j.rinp.2022.105505

25. Getto E, Sun K, Was GS. Characterization of M2X formed during 5áMeV Fe2+ irradiation. J Nucl Mater. 2017;485:154–158. https://doi.org/10.1016/j.jnucmat.2016.12.027

26. Wang X, Yan Q, Was GS, Wang L. Void swelling in ferritic-martensitic steels under high dose ion irradiation: Exploring possible contributions to swelling resistance. Scripta Materialia. 2016;112:9–14. https://doi.org/10.1016/j.scriptamat.2015.08.032

27. Hou X et al. Microstructure and electronic structure of Cr2C and Fe2Y in the Cr-coating prepared by pack-cementation on the surface of ODS steel. Mater Today Commun. 2021;28:102591. https://doi.org/10.1016/j.mtcomm.2021.102591

28. Tanaka R, Shinoda T, Ishii T. On the hexagonal carbide V2C precipitated in austenitic steels. Tetsu-to-Hagané. 1970;56(10):1406–1408. https://doi.org/10.2355/tetsutohagane1955.56.10_1406

29. Bowman AL, Wallace TC, Yarnell JL, Wenzel RG, Storms EK. The crystal structures of V2C and Ta2C. Acta Crystallographica. 1965;19(1):6–9. https://doi.org/10.1107/S0365110X65002670

30. Chong X, Jiang YH, Zhoua R, Feng J. Electronic structures mechanical and thermal properties of V–C binary compounds. RSC Adv. 2014;4(85):44959–44971. https://doi.org/10.1039/C4RA07543A

31. Suetin DV, Shein IR, Ivanovskii AL. Elastic and electronic properties of hexagonal and cubic polymorphs of tungsten monocarbide WC and mononitride WN from first-principles calculations. Phys Status Solidi B. 2008;245(8):1590–1597. https://doi.org/10.1002/pssb.200844077

32. Jain A et al. Commentary: the materials project: a materials genome approach to accelerating materials innovation. APL Mater. 2013;1(1). https://doi.org/10.1063/1.4812323

33. Li Y et al. Theoretical study on the stability, elasticity, hardness and electronic structures of W–C binary compounds. J Alloys Compd. 2010;502(1):28–37. https://doi.org/10.1016/j.jallcom.2010.04.184

34. Liu Y, Jiang YH, Feng J, Zhou R. Elasticity, electronic properties and hardness of MoC investigated by first principles calculations. Physica B Condens Matter. 2013;419:45–50. https://doi.org/10.1016/j.physb.2013.03.016

35. Shohoji N et al. Formation of hexagonal η-MoC1−x phase at a temperature lower than 1660°C by solar radiation heating under presence of excess free carbon. Int J Refract Metals Hard Mater. 2007;25(3):220–225. https://doi.org/10.1016/j.ijrmhm.2006.05.004

36. Hillert M, Qiu C. A reassessment of the Fe-Cr-Mo-C system. J Phase Equilibria. 1992;13:512–521. https://doi.org/10.1007/BF02665764

37. Wu L et al. Understanding the mechanical properties of vanadium carbides: Nano-indentation measurement and first-principles calculations. J Alloys Compd. 2013;548:60–64. https://doi.org/10.1016/j.jallcom.2012.09.014

38. Xie C, Liu N, Cheng X, Li D, Zeng Q. Discovering novel VC1−x compounds through hybrid first-principles and evolutionary algorithms. J Euro Ceram Soc. 2016;36(15):3593–3599. https://doi.org/10.1016/j.jeurceramsoc.2016.03.034

39. Chong X, Jiang Y, Feng J. Exploring the intrinsic ductile metastable Fe-C compounds: Complex chemical bonds, anisotropic elasticity and variable thermal expansion. J Alloys Compd. 2018;745:196–211. https://doi.org/10.1016/j.jallcom.2018.02.140

40. Guziewski M. Multiscale study of the pearlitic microstructure in carbon steels: atomistic investigation and continuum modeling of iron and iron-carbide interfaces [PhD thesis]. Colorado State University; 2018.

41. Zhang D et al. The structural, magnetic, electronic, and mechanical properties of orthogonal/hexagonal M7C3 (M = Fe and Cr) carbides from first-principles

calculations. Vacuum. 2022;203:111175. https://doi.org/10.1016/j.vacuum.2022.111175

42. Chong X et al. Tailoring the anisotropic mechanical properties of hexagonal M7X3 (M=Fe, Cr, W, Mo; X=C, B) by multialloying. Acta Materialia. 2019;169:193–208. https://doi.org/10.1016/j.actamat.2019.03.015

43. Xiao B, Feng J, Zhou CT, Jiang YH, Zhou R. Mechanical properties and chemical bonding characteristics of Cr7C3 type multicomponent carbides. J Appl Phys. 2011;109(2). https://doi.org/10.1063/1.3532038

44. Xiao B et al. A comparative study of Cr7C3, Fe3C and Fe2B in cast iron both from ab initio calculations and experiments. J Phys D Appl Phys. 2009;42(11):115415. https://doi.org/10.1088/0022-3727/42/11/115415

45. He Ret al. Experimental study of covalent Cr3C2 with high ionicity: Sound velocities, elasticity, and mechanical properties under high pressure. Scripta Materialia. 2023;224:115146. https://doi.org/10.1016/j.scriptamat.2022.115146

46. Ohmori Y. χ-carbide formation and its transformation into cementite during the tempering of martensite. Trans Jpn Inst Metals. 1972;13(2):119–127. https://doi.org/10.2320/matertrans1960.13.119

47. Dirand M, Afqir L. Identification structurale precise des carbures precipites dans les aciers faiblement allies aux divers stades du revenu, mecanismes de precipitation. Acta Metallurgica. 1983;31(7):1089–1107. https://doi.org/10.1016/0001-6160(83)90205-5

48. Chong X, Jiang YH, Zhou R, Feng J. First principles study the stability, mechanical and electronic properties of manganese carbides. Comput Mater Sci. 2014;87:19–25. https://doi.org/10.1016/j.commatsci.2014.01.054

49. Leineweber A, Shang S, Liu Z-K, Widenmeyer M, Niewa R. Crystal structure determination of Hägg carbide, χ-Fe5C2 by first-principles calculations and Rietveld refinement. Zeitschrift für Kristallographie. 2012;227(4):207–220. https://doi.org/10.1524/zkri.2012.1490

50. Liu W-H et al. The mechanical and electronic properties of o-Fe2C, h-Fe3C, t-Fe5C2, m-Fe5C2 and h-Fe7C3 compounds: First-principles calculations. Physica B Condens Matter. 2021;606:412825. https://doi.org/10.1016/j.physb.2021.412825

51. Rapposch M, Kostiner E, Wayne SF, Nowotny H. Die Kristallstruktur von Molybdän-Zementit, Mo 12 Fe 22 C 10 (ξ-Phase). Monatshefte für Chemie Chem Monthly. 1985;116:1237–1245. https://doi.org/10.1007/BF00811096

52. Ghosh G. A first-principles study of cementite (Fe3C) and its alloyed counterparts: elastic constants, elastic anisotropies, and isotropic elastic moduli. AIP Adv. 2015;5(8). https://doi.org/10.1063/1.4928208

53. Echeverri Restrepo S. Density functional theory characterisation of cementite (Fe3C) with substitutional molybdenum (Mo) atoms. Physica B Condensed Matter. 2022;631:413669. https://doi.org/10.1016/j.physb.2022.413669

List of Symbols, Abbreviations, and Acronyms

AISI	American Iron and Steel Institute
BCC	body-centered cubic
CALPHAD	Calculation of Phase Diagram
CCA	complex concentrated alloy
DFT	density functional theory
FCC	face-centered cubic
HCP	hexagonal close-packed
ID	identification
LIT	literature
MD	molecular dynamics
ML	machine learning
NSD	nucleation site density
OR	orientation relationship
Ref.	reference
SG	space group
SHP	simple hexagonal phase
T-C	Thermo-Calc
TEM	transmission electron microscopy
TTT	time–temperature–transformation
UHSS	ultra-high strength steel
V	volume
VM	molar volume
XRD	X-ray diffraction

1 (PDF)	DEFENSE TECHNICAL INFORMATION CTR DTIC OCA
1 (PDF)	DEVCOM ARL FCDD RLB CI TECH LIB